Research Square

Preprints are preliminary reports that have not undergone peer review.
They should not be considered conclusive, used to inform clinical practice,
or referenced by the media as validated information.

Comparative Numerical Analysis of Chemically Reactive MHD Functional Nanofluid Coating Flow over Cone and Wedge Geometries

Pavithra G. B
GITAM University
V. Nagaradhika
nagaradhika79@gmail.com
Sir M. Visvesvaraya Institute of Technology
S Manjunatha
Sai Vidya Institute of Technology
O. Anwar Bég
MPESG, Salford University
T. A. Beg
Israfil House
S. Kuharat
MPESG, Salford University

Research Article

Keywords: Nanofluid, MHD, thermal radiation, cone and wedge, heat source, activation energy, nano-coating manufacture, chemical reactions, RSM

Posted Date: October 5th, 2026

DOI: https://doi.org/10.21203/rs.3.rs-10980045/v1

License: This work is licensed under a Creative Commons Attribution 4.0 International License.
Read Full License

Additional Declarations: No competing interests reported.

Comparative Numerical Analysis of Chemically Reactive MHD Functional Nanofluid Coating Flow over Cone and Wedge Geometries

Pavithra G.B [1], V. Nagaradhika [2*], Manjunatha S [3], O. Anwar Bég[4], T.A. Beg [5], S. Kuharat[4]

[1] *Government First Grade College, Gundlupete-571111, India.*
[1]*Department of Mathematics, GSS, GITAM Deemed to be University, Benguluru-561203, India.*
[2*] *Department of Mathematics, Sir M Visvesvaraya Institute of Technology, Bengaluru -562 157, India.*
[3] *Department of Mathematics, Sai Vidya Institute of Technology, Bangalore, Karnataka, 560064, India.*
[4] *MPESG, Dept. of Aeronautical & Mechanical Engineering, Corrosion Lab, 3-08, SEE Building, Salford University, Manchester, M54WT, UK.*
[5]*Engineering Mechanics Research, Israfil House, Manchester, M13 OYW, UK.*
Corresponding author: nagaradhika79@gmail.com

ABSTRACT

Coating flows of electro-conductive functional magnetic nanofluids external to both wedge and cone shapes embedded in porous media under external magnetic field modulation are investigated theoretically and numerically. Chemical reaction, thermal radiation, heat generation and activation energy effects are included in the mathematical model. Buongiorno's two-component nanoscale model is deployed to evaluate mass diffusion phenomena of the nanoparticles under thermophoretic and Brownian motion effects. A separate species equation is included for reactive solute diffusion. By making use of suitable similarity transformation techniques, the original system of partial differential equations is reduced to a system of nonlinear ordinary differential equations with suitable wall and free stream boundary conditions. The MATLAB 'bvp4c' solver is used to numerically solve the nonlinear dimensionless ordinary differential boundary value problem. Verification with previous studies is included. The influence of key emerging parameters on velocity and temperature is displayed graphically. Response Surface Methodology (RSM) is then deployed to conduct statistical analysis and optimize the transport process for skin friction, Nusselt number (heat transfer rate), solutal Sherwood number (solute mass transfer rate) and nanoparticle Sherwood number. The results show that for both the cone and wedge geometries, flow acceleration is produced with decreasing Richardson numbers. Increasing Brownian motion parameter generates strong micro-convection currents in the base fluid, increasing the overall thermal conductivity and enhancing temperature and associated thermal boundary layer thickness. Increasing thermophoresis parameter intensifies thermal diffusion and elevates temperatures, reduces nanoparticle volume fraction and decreases nanoparticle species boundary layer thickness. An elevation in internal heat-generating and Rosseland radiation-conduction parameter both contribute significantly to the dramatic rise in temperature. With enhanced R^2 values of 98.56% for the cone and 99.04% for the wedge, the nanoparticle Sherwood number achieves a high level of prediction accuracy. The simulations are relevant to coating flows of biochemical engineering devices with functional nano-liquids.

KEYWORDS: Nanofluid, MHD, thermal radiation, cone and wedge, heat source, activation energy, nano-coating manufacture, chemical reactions, RSM.

NOMENCLATURE:

Cf	Skin friction	Ri	Richardson number
Cp	Specific heat of the fluid (J/kgK)	Sc	Schmidt number
C_w, C_∞	Wall and ambient concentration conditions (kg/m^3)	T_w, T_∞	Wall and ambient temperature conditions (K)
D_B	Brownian diffusion coefficient (m^2/s)	Nt	Thermophoresis parameter
D_T	thermophoretic diffusivity (m^2/s)	G	Temperature function
E	Activation energy	H	Solute concentration
g	Acceleration due to gravity (m/s^2)	S	Nanoparticle concentration
Gr	Grashof number	**Greek letters**	
K	Porous medium permeability (m^2)	τ	Heat capacities of nanoparticles to the fluid ratio
Kr	Chemical reaction parameter	ρ_f	Nanofluid density (kg/m^3)
k_f	Thermal conductivity (W/mK)	η	Non-dimensional coordinate
Le	Lewis number	σ_f	Electrical conductivity (S/m)
M	Magnetic field	ϕ_w, ϕ_∞	wall and ambient nanoparticle concentration conditions
Nb	Brownian motion parameter	ν_f	kinematic viscosity (m^2/s)
Nc	buoyancy ratio parameter of species	μ_f	Dynamic viscosity (kg/ms)
Nr	nanoparticle buoyancy ratio parameter	**Subscripts**	
Pr	Prandtl number	tnf	Ternary nanofluid
Q	Heat source parameter	hnf	Hybrid nanofluid
R	Thermal radiation parameter	nf	nanofluid
Re	Reynolds number	f	Base fluid

1.INTRODUCTION

Fluid dynamics is a large field of study since it has applications in practically every engineering discipline, including aerospace, chemical, civil, mechanical and biomedical engineering. Coating flow of cones and wedges [1] describes how viscous fluids (like paints, liquid foods, or polymers) spread over surfaces that are angled or conical. The fluid spreads driven by gravity, centrifugal force, or pressure, balancing viscous resistance and surface tension. These flows differ fundamentally in boundary layer shape, velocity profile, and heat/mass transfer rates. Significant interest in coating fluid dynamics of cones/wedges and also cone-wedge hybrid geometries has been stimulated by the relevance of such geometries to a range of chemical, biochemical and process mechanical engineering systems [2, 3].

Magnetohydrodynamics (MHD) is the study of electrically conducting fluids (like molten metals and ionized gases) in magnetic fields. In manufacturing, it is a critical technology used to control, pump, stir, and shape liquid metals without physical contact, drastically improving efficiency and material quality [4]. Magnetohydrodynamics (MHD) in coating flow involves applying a transverse magnetic field to electrically conductive, Newtonian or non-Newtonian fluids during processes like wire, blade, roll or enrobing coating [5]. This technique uses Lorentz forces to exert precise, contactless control over the fluid velocity and pressure gradient, allowing engineers to finely regulate final coating thickness and homogeneity. When managing an MHD coating system, one can essentially balancing the fluid viscous/elastic resistance against the applied magnetohydrodynamic (Lorentzian) drag. By tuning the magnetic field, engineers can directly adjust the volume of fluid transferred to the substrate. Stronger magnetic fields typically result in a thicker, heavier coating load depending on the coater geometry [6]. MHD acts as a stabilizing mechanism for these complex viscoelastic fluids, helping to prevent dripping or uneven pooling before the coating is cured. External boundary layer flows from wedges are often termed Falkner-Skan flows. Wedge flows introduce a pressure gradient governed by the wedge angle parameter (Hartree pressure gradient). The geometry accelerates or decelerates the boundary layer, altering the local skin friction and heat transfer differently depending on whether the flow is a favourable or adverse pressure gradient. A conical geometry tends to restrict the boundary layer thickness more than flat plates, leading to distinct heat transfer rates and temperature gradients. A number of interesting studies have addressed magnetohydrodynamic coating flows of cones and or/wedge geometries. Vajravelu and Nayfeh [7] examined the external hydromagnetic coating flow of a viscous Newtonian liquid on a vertical cone or wedge with free convection and heat generation/absorption. They deployed a finite difference method and showed that heat source and magnetic field strength produce significant modifications in boundary layer characteristics. Chamkha [8] extended the model in [7] to consider porous media drag effects. Gaffar et al. [9] considered non-isothermal wall effects in electromagnetic tangent hyperbolic polymer flow from an upright porous cone. Gaffar et al. [10] further studied the effects of convective wall heating on Falkner-Skan flow of magnetic non-Newtonian polymers along a wedge with variable wall temperature and mixed convection.

In recent years, engineers have explored the use of nanomaterials in coating technologies. Nanoparticles in coating flows provide critical rheological control and structural reinforcement. They act as nano-ball-bearings to improve flowability during application and

form dense networks that cure into multifunctional, durable thin films. Nanoparticles may be metallic (e.g. zinc, copper etc), metallic oxides (magnesium oxide, iron oxide etc) or carbon-based (graphite, graphene, graphene oxide, silica, silicon dioxide etc) or combinations of these types. Their judicious integration revolutionizes surface protection, scratch resistance, and optical clarity. he extremely high surface-area-to-volume ratio of nanoparticles affects interfacial forces. Adding the correct surface functionality (via specific resins or ligands) allows nanoparticles to disperse uniformly, preventing clumping and stabilizing the liquid before it sets. Nano-coatings [11] offer numerous advantages, including surface hardness, adhesive strength, long-term and/or high-temperature corrosion resistance, the enhancement of tribological properties, etc. In addition, nano-coatings can be applied in thinner and smoother thickness, which allows flexibility in equipment design, improved efficiency, lower fuel economy, lower carbon footprints, and lower maintenance and operating costs. Nano-coatings are utilised efficiently to reduce the effect of a corrosive environment. A nanocoating is a coating that either has constituents in the nanoscale or is composed of layers that are less than 100 nm. The fine sizes of nanomaterials and the high density of their ground boundaries enable good adhesion and an excellent physical coverage of the coated surface. An important category of nanomaterials known as nanofluids have emerged as a significant area of interest in the 21st century. Nanofluids are engineered suspensions of nanoparticles in base liquids and are revolutionizing coatings by enhancing properties like thermal conductivity, corrosion resistance, and hydrophobicity. Compared to traditional coolants, nanofluids exhibit vastly superior thermophysical properties. Since nanoparticles have an exceptionally high surface-area-to-volume ratio, they act as miniature heat carriers and create micro-convection currents within the fluid [12]. Key developments in nanofluid technology were pioneered by Choi [13]. Important models for simulating nanofluids are the Buongiorno model [14] and Tiwari-Das model [15]. The Buongiorno nanofluid model is a widely used two-component mathematical framework in thermal engineering. Developed by MIT professor Jacopo Buongiorno in 2006, it explains how nanoparticles (usually under 100 nm) enhance heat and mass transfer in base fluids, primarily focusing on two key mechanisms: Brownian motion (random, chaotic collision and movement of nanoparticles suspended in the liquid occur and this micro-mixing improves thermal conductivity and energy dispersion) and thermophoresis (movement of nanoparticles from hotter regions to cooler regions due to temperature gradients. The Buongiorno model is particularly useful as it incorporates these slip-mechanisms, which traditional single-phase fluid models such as the Tiwari-Das model cannot account for. The Tiwari-Das nanofluid model is a single-phase mathematical framework which assumes that the

solid nanoparticles are uniformly dispersed within a base fluid. It focuses on how the nanoparticle solid volume fraction of these nanoparticles alters the overall thermophysical properties of the working fluid but does not feature the sophisticated slip mechanisms of the Buongiorno model, although it is a more robust approach for studying specific nanomaterial types. Both models have been extensively reviewed by Bég [16] in the context of coating flows, emphasizing that nanoparticles allow coatings to dissipate heat, withstand harsh environments, and self-clean without adding significant weight or bulk. Incorporating nanofluids into coating formulations creates specialized, multi-functional surfaces with high-performance characteristics. Suspensions of metallic oxides (alumina, titania etc) or carbon-based nanoparticles in resins boost the thermal conductivity of the coating, effectively dissipating heat from electronics, automotive parts, and industrial machinery. Hybrid nanofluids (like Copper-MXene composites) control the release of toxic ions and lower surface energy to prevent bacterial or marine organism adhesion as noted by Huang et al. [17]. While nanofluids deploying different nanoparticles and base fluids (lubricants, polymers etc) offer remarkable performance gains, they face a few key challenges. High concentrations can increase the viscosity of the coating material, which complicates application and raises costs, as nanoparticle formulations span a wide pricing spectrum. Furthermore, maintaining long-term suspension stability to prevent sedimentation and agglomeration requires careful formulation. Magnetic nanoparticles are a more complex subset of nanoparticles which enable greater functionality of the coatings and can achieve superior durability and resilience in a plethora of applications including surface deposition and coatings [18, 19, 20]. Several investigators have studied magnetic nanofluid coating flows on wedges and cones. Gorla et al. [21] used the Nakamura tridiagonal method to compute Buongiorno nanofluid mixed convection boundary layer flow from a vertical wedge embedded in a porous medium saturated with a nano fluid. They showed that as Brownian motion parameter is elevated friction factor and surface mass transfer rates increase whereas heat transfer rate (Nusselt number) decreases, and that with greater thermophoresis parameter mass transfer rate (Sherwood number) decreases. They also noted that with greater Lewis number, heat transfer rate decreases and mass transfer rate increases, whereas with larger wedge angle both heat and mass transfer rates increase. Umavathi et al. [22] used MATLAB software to compute the steady, incompressible dissipative boundary-layer flow of a non-Newtonian micropolar nanofluid over a wedge-geometry. They used the Tiwari-Das model and considered copper, diamond, silver and titanium dioxide nanoparticles. They noted that thermal boundary layer thickness is enhanced with Eringen micropolar vortex viscosity parameter and nanoparticle volume fraction and

velocity is boosted with increasing nanoparticle volume fraction. They further noted that temperature is elevated with increase in heat source but reduced with heat sink, and that skin friction is boosted with pressure gradient parameter whereas Nusselt number is depleted. Nusselt number is observed to be a maximum for diamond whereas it is a minimum for silver. Temperatures were also computed to be a maximum for silver and progressively lower for copper, diamond and with a minimum for titania. Further studies include Chamkha et al. [23] (on wedge flow in nanofluid-saturated porous media), Sandeep and Reddy [24] (copper-water nanofluid flow from cones and wedges in a magnetic field with thermal radiation flux) and Das et al. [25] (on slip Buongiorno gyrotactic nanofluid boundary layer flows in cone-disk systems). Ray et al. [26] used a homotopy method to simulate power-law non-Newtonian cone, wedge and plate boundary layer flows. They showed that with higher thermal and solute Grashof numbers strong flow acceleration is produced whereas temperature and nanoparticle volume fraction are reduced for all three different configurations, i.e., cone, wedge and plate. Furthermore, the thermal and concentration boundary layers are more dramatically modified for the wedge case, as compared to the plate and cone. Salawu et al. [27] computed the ternary Prandtl-Eyring magnetic hybrid nanofluid coating flow over a stretching wedge with spherical titanium dioxide, cylindrical magnesium oxide and platelet aluminium nanoparticles.

In nanofluid coating manufacturing processes, chemical reactions often arise. Nanocoating manufacture relies on precise chemical reactions to build ultrathin, functional layers at the atomic or molecular scale. The primary manufacturing techniques use hydrolysis, condensation, thermal decomposition, and polymerization to engineer these surfaces. Chemical reactions in coatings drive the curing process—transforming liquid paint into a solid, durable protective layer—rather than relying just on solvent evaporation. Key reactions include polyurethane crosslinking (isocyanates reacting with polyols), epoxy curing (amines or anhydrides opening oxirane rings), and oxidative crosslinking (alkyd resins reacting with atmospheric oxygen). To simulate the effects of chemical reactions, mathematical mass transfer (species diffusion) models are required [28]. Activation energy effects in nano-coatings are critical for understanding how these materials form, degrade, and interact with their environments. Two primary contexts define these effects: thermodynamic activation during the coating's formulation and the surface-level activation energy barriers during its operational use. During the formulation or heat treatment of a nanocoating, activation energy dictates the speed and temperature at which the material crystallizes, oxidizes, or cures. Nanomaterials typically have a high surface-area-to-volume ratio, making them susceptible to surface-initiated grain

growth. Nano-coatings (e.g., amorphous alumina) are often engineered with higher activation energy barriers intentionally designed to suppress this grain growth, stabilizing high-performance states (like high-conductivity cubic phases) at elevated operating temperatures. The addition of nanoparticles (e.g. Nickel oxide) to polymer-based matrices generally decreases the activation energy required for thermal decomposition, meaning degradation initiates at lower temperatures. Precise mixing and dispersion are required to control this effect. In coating mass transfer, activation energy dictates the energy barrier required for chemical species to diffuse or react. Higher activation energy suppresses mass diffusion, slows down reaction rates, and causes reactant accumulation. In contrast, lower activation energy accelerates coating formation. Mass transfer in coating processes (such as polymer curing, electrodeposition, or spin-coating) typically follows Arrhenius kinetics, where the reaction rate or diffusion coefficient scales exponentially with temperature. The impact of activation energy on the coating mass transfer rate depends on whether the process is governed by chemical reactions (kinetically controlled) or mass transport (diffusion controlled). Several researchers have analysed nanofluid coating flows on wedges and cones with reactive and activation energy physiochemical effects. Zainal et al. [29] reported that increasing the nanoparticle volume from 0% to 1% raises the skin friction coefficient by 1.6% to 3.2%. However, including activation energy in the model reduces the mass transfer rate and flattens the concentration curve. Singh et al. [30] simulated MHD sodium alginate ternary nanofluid flow on both conical and wedge geometries. They considered exothermic/endothermic chemical reactions and showed that exothermic reactions typically enhance thermal energy (increasing temperature profiles), whereas endothermic reactions absorb heat, leading to temperature drops within the boundary layer. They further noted that solute concentration profiles are enhanced with activation energy parameter, Nusselt number at the wall is reduced with increasing chemical reaction rates and is 48.68% higher for the wedge than the cone geometry for the exothermic case and 35.57% in the endothermic case. They additionally observed that Sherwood number (mass transfer rate) for the cone exceeds that for the wedge by 7.83% in the exothermic case and 19.27% in the endothermic case. Further investigations of reactive coating flows include Krishna and Reddy [31] (who considered viscoplastic magnetic fluids), Shammari et al. [32] (on oscillatory coating flow of a cone in non-Darcy porous media), Zhang et al. [33] (on spectral computation of magnetized nanofluid coating with activation energy and wall suction), Shanmugapriya et al. [34] (on viscoelastic Jeffrey ternary hybrid nanofluid wedge coating flow with catalytic reactions) and Li et al. [36] (on tangent hyperbolic bioconvection nanofluid flow from a magnetic sensor wedge with wall suction). These studies have confirmed that chemical

reactions and Arrhenius kinetics exerts a significant role in coating transport processes of conical bodies and wedge geometries. Other complex multi-physics studies of cone and wedge geometries have featured rough wall effects [36], graphene oxide combined with molybdenum disulfide hybrid nanoparticles [37] and thermal relaxation (non-Fourier heat conduction) [38].

In modern coating processes, the presence of a porous medium produces resistance to the motion of the fluid, which influences the velocity distribution and its transport characteristics [39]. This can be exploited in filtration-based control in nano-coatings. Porous media control coating flows by leveraging permeability and capillary action to regulate fluid velocity, distribute liquid evenly, and filter out defects. They prevent film rupture and stabilize the coating bead, ensuring a uniform, defect-free layer [40]. Controlling coating flows with porous media relies on two main mechanisms: passive flow resistance (slowing flow speed) and active capillary penetration (absorbing or redistributing liquid). Porous media hydrodynamic models are diverse and include drag force, spatially periodic, volume averaged and others. The Darcy model and Darcy-Brinkman models remain the most popular approach in coating boundary layer flows due to their simplicity and accuracy at low Reynolds numbers. Recent studies implementing these models include Padmaja et al. [41] (on copper-aqueous magnetic nanofluids in vertical cone spin coating in Darcy-Brinkman porous media), Uddin et al. [42] (on pseudoplastic/dilatant nanofluid coating flow in Darcian porous media with heat source effects) and Bég et al. [43] hydromagnetic convective boundary layer flow from a spinning cone in anisotropic permeable porous media).

An inspection of the literature has shown that computational studies investigating the composite effects of activation energy, chemical reaction, magnetic field modulation, thermal and multi-species buoyancy (associated with nanoparticles and solute), thermal radiation and internal heat source on external coating hybrid electroconductive functional nanofluid flows on either wedge or cone geometries embedded in porous media, are very sparse. These are the novelties and focal points of the present work. Buongiorno's two-component nanoscale model is deployed to evaluate mass diffusion phenomena of the nanoparticles under thermophoretic and Brownian motion effects. A separate species equation is included for reactive solute diffusion. Via appropriate similarity transformations, the primitive nonlinear partial differential conservation equations with wall and free stream boundary conditions are rendered dimensionless and converted into a strongly coupled, ninth order nonlinear ordinary differential boundary value problem. A computational solution is presented via the robust MATLAB

'bvp4c' solver [44]. Validation with previous studies is included. The impact of all key emerging parameters on velocity, temperature, skin friction, Nusselt number (heat transfer rate), solutal Sherwood number (solute mass transfer rate) and nanoparticle Sherwood number is visualized graphically. Response Surface Methodology (RSM) [45] is then deployed to conduct statistical analysis and optimize the nanofluid coating transport process.

2. MATHEMATICAL FORMULATION

Magnetic nanofluid functional coating boundary layer flow external to two different stretching geometries i.e. a wedge and a cone. Laminar, steady-state, incompressible mixed convective transport is assumed. Velocity aligned with the cone/wedge wall in the x-direction is designated by u and velocity transverse to the wall in the y-direction is denoted by v, respectively, in this study. Figure 1 displays the physical model and coordinate system. The geometric features encompass the half-angle (γ), full-angle (χ) and radius (r) of the wedge and cone, respectively.

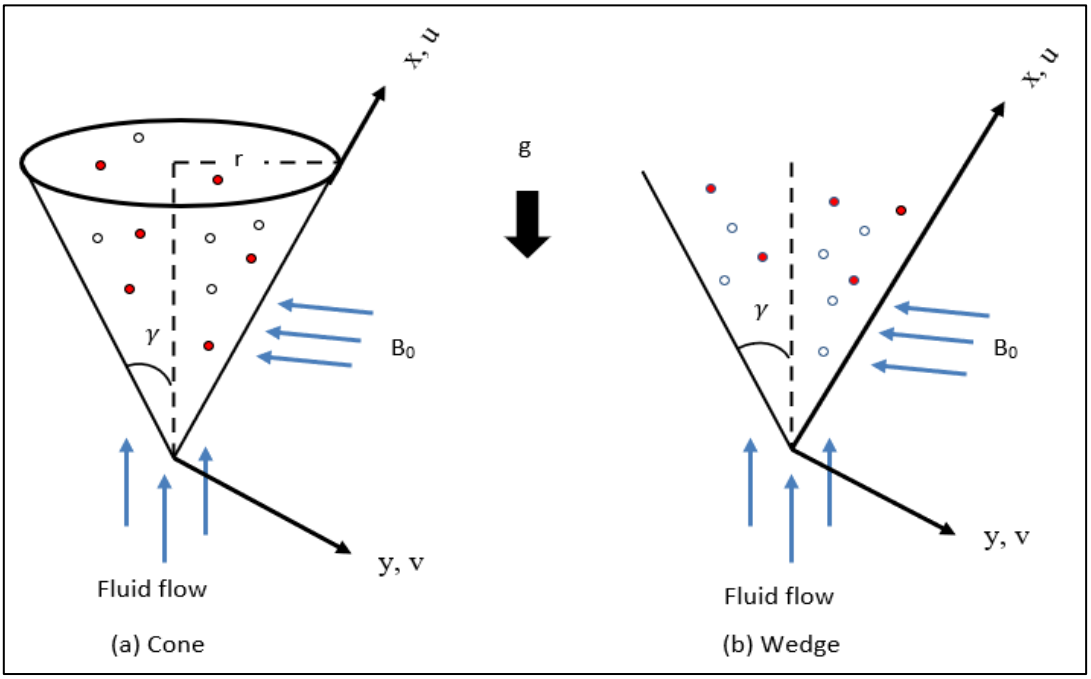


Figure 1: Physical model for functional nanofluid coating flow on a cone and wedge.

A transverse (or radial) magnetic field B0 is imposed external to the wedge or cone and is static and uniform. Magnetic induction effects are neglected. It is presumed that the spherically shaped TiO_2, Cu and Fe_2O_4 nanoparticles are distributed throughout propylene glycol ($C_3H_8O_2$) base fluid. The coating transport problem is described by generalizing and amalgamating the earlier models of Hussain et al. [46], Hassanien et al. [47] and Kulkarni et al. [48]:

Continuity equation:

$$\left(ur^m\right)_x + \left(vr^m\right)_y = 0, \tag{1}$$

Momentum equation:

$$uu_x + vu_y = \nu_{tnf} u_{yy} + g(1-\phi_\infty)\left[\beta_t(T-T_\infty) + \beta_c(C-C_\infty) - \left(\frac{\rho_p - \rho_f}{\rho_f}\right)(\phi-\phi_\infty)\right]cos(\gamma) - \frac{\mu_{tnf}}{\rho_{tnf}K*}u - \frac{\sigma_{tnf}B_0^2}{\rho_{tnf}}u, \tag{2}$$

Energy equation:

$$uT_x + vT_y = \alpha_{tnf}T_{yy} + \tau\left(D_B\phi_y T_y + \frac{D_T}{T_\infty}\left(T_y\right)^2\right) + \frac{1}{\left(\rho C_p\right)_{tnf}}\left(q_r\right)_y + \frac{Q_1}{\left(\rho C_p\right)_{tnf}}\left(T-T_\infty\right), \tag{3}$$

Solute concentration equation:

$$uC_x + vC_y = D_B C_{yy} - K_1^2\left(C-C_\infty\right)\left(\frac{T}{T_\infty}\right)^n \exp\left(\frac{-E_{a_1}^*}{K_1^* T}\right), \tag{4}$$

Nanoparticle volume fraction conservation equation:

$$u\phi_x + v\phi_y = D_B\phi_{yy} + \frac{D_T}{T_\infty}T_{yy}, \tag{5}$$

Here all parameters are defined in the notation. In Eqn. (4), Ea defines activation energy, K1 is the pre-exponential factor, which constitutes the constant rate of homogenous chemical reaction, k* = 8.61 × 10− 5J/K denotes the Boltzmann constant and n is the temperature power-law exponent. The following boundary constraints at the wall and the freestream are imposed [49]:

Wall: $u = U_w(x) + B_1\ u_y, v = 0, T = T_w, C = C_w, \phi = \phi_w,$ at $y = 0$

Freestream: $u \to 0, v \to 0, T \to T_\infty, C \to C_\infty, \phi \to \phi_\infty$ as $y \to \infty$. (6)

Here B1 is the wall stretching rate. Next, the following similarity transformations are invoked [46, 47, 48]:

$$v = \frac{-\nu_f(m+1)}{l}f(\eta),\ u = \frac{x\nu_f}{l^2}f'(\eta),\ \eta = \frac{y}{l}, G(\eta) = \frac{T-T_\infty}{T_w-T_\infty},$$
$$H(\eta) = \frac{C-C_\infty}{C_w-C_\infty},\ S(\eta) = \frac{\phi-\phi_\infty}{\phi_w-\phi_\infty} \tag{7}$$

Here f is stream function, G is dimensionless temperature, H is dimensionless solute concentration, S is dimensionless nanoparticle volume fraction, η is transverse similarity variable (dimensionless y-coordinate), l is the length of the wedge/cone wall, m is the Hartree pressure gradient parameter. The model incorporates two distinct geometries, namely the wedge and the cone, under the following assumptions:

$$\begin{aligned} &m = 0 \text{ and } \gamma \neq 0 \rightarrow \text{Wedge} \\ &m = 1 \text{ and } \gamma \neq 0 \rightarrow \text{Cone} \end{aligned} \tag{8}$$

Substituting the scaling variables from Eq. (7), into Eqns. (2) to (5) leads to the dimensionless velocity, thermal, solute and nanoparticle concentration boundary layer equations, and the mass conservation equation is automatically satisfied:

$$\begin{aligned} &\frac{A_1}{A_2} F'''(\eta) + (1+m) F(\eta) F''(\eta) - \left(F'(\eta)\right)^2 + Ri\left(G(\eta) + NcH(\eta) - NrS(\eta)\right)\cos(\gamma) \\ &-\frac{A_1}{A_2} KF'(\eta) - \frac{A_3}{A_2} MF'(\eta) = 0 \end{aligned} \tag{9}$$

$$\frac{(A_4 + R)}{A_5} G''(\eta) + \Pr\left((1+m) F(\eta) G'(\eta) + NbS'(\eta) G'(\eta) + Nt\left(G'(\eta)\right)^2 + \frac{Q}{A_5} G(\eta) \right) = 0 \tag{10}$$

$$H''(\eta) + Sc(1+m) F(\eta) H'(\eta) - ScKr\left(1 + \delta G(\eta)\right)^n \exp\left(-E/\left(1 + \delta G(\eta)\right)\right) = 0 \tag{11}$$

$$S''(\eta) + Le(1+m) F(\eta) S'(\eta) + \frac{Nt}{Nb} G''(\eta) = 0 \tag{12}$$

Here A1…A5 are nanofluid property ratios. The emerging non-dimensional boundary conditions are:

$$\begin{aligned} &F(\eta) = 0, F'(\eta) = 1 + B_1 F''(\eta), G(\eta) = 1, H(\eta) = 1, S(\eta) = 1 \text{ at } \eta = 0 \\ &F'(\eta) \rightarrow 0, G(\eta) \rightarrow 0, H(\eta) \rightarrow 0, S(\eta) \rightarrow 0 \text{ as } \eta \rightarrow \infty \end{aligned} \tag{13}$$

Here the non-dimensional parameters take the following definitions:

$$Nr = \frac{(\rho - \rho_f)(\phi_w - \phi_\infty)}{\rho_f \beta_t (T_w - T_\infty)(1 - \phi_\infty)}, Nc = \frac{\beta_c (C_w - C_\infty)}{\beta_t (T_w - T_\infty)}, Pr = \frac{\nu_f}{\alpha_m}, Le = \frac{\nu_f}{D_B}, Ri = \frac{Gr}{Re^2},$$
$$Sc = \frac{\nu_f}{D_B}, E = \frac{E_{a1}^*}{K_1^* T_\infty}, Kr = \frac{l^2 K_1^2}{\nu_f}, Nb = \frac{\tau D_B l^2 (\phi_w - \phi_\infty)}{\nu_f}, M = \frac{\sigma_f B_0^2 l^2}{\rho_f \nu_f}, K = \frac{l^2}{K*},$$

$$Nt = \frac{\tau D_B l^2 (T_w - T_\infty)}{T_\infty \nu_f}, Gr = \frac{g\beta_t (T_w - T_\infty)(1-\phi_\infty)x^3}{\nu_f^2}, R = \frac{16\sigma^* T_\infty^3}{3k^* k_f}, Q = \frac{Q_1 l^2}{(\rho C_p)_f \nu_f} \quad (14)$$

In Eqn. (14) Nr is buoyancy ratio (nanoparticle buoyancy force to thermal buoyancy force ratio), Nc is solute buoyancy ratio (solute buoyancy force to thermal buoyancy force ratio), Pr is Prandtl number, Le is Lewis number, Ri is Richardson number, Sc is Schmidt number, E is activation energy parameter, Kr is first order homogenous chemical reaction parameter, Nb is Brownian motion parameter, M is a magnetic interaction parameter (ratio of Lorentzian magnetic force to inertial body force), Nt is thermophoretic parameter, Gr is thermal Grashof number, K is permeability parameter, R is the radiation-conduction number and Q is heat source parameter.

Important wall characteristics for coating flows are the wall shear stress, heat transfer rate, solute mass transfer rate and nanoparticle mass transfer rate. These are defined as follows.

Wall shear stress:

$$\mathrm{Re}\, Cf = \frac{\tau_w}{\rho_f u_w^2} = A_1 f''(0) \quad (15)$$

Rate of heat transfer (Nusselt number)

$$\mathrm{Re}^{-1/2}\, Nu = \frac{x q_w}{k_f \left(T_w - T_\infty\right)} = -A_4 G'(0) \quad (16)$$

Rate of solute mass transfer (solute Sherwood number)

$$\mathrm{Re}^{-1/2}\, Sh = \frac{x J_w}{D_B \left(C_w - C_\infty\right)} = -H'(0) \quad (17)$$

Rate of nanoparticle mass transfer (nanoparticle Sherwood number):

$$\mathrm{Re}^{-1/2}\, Shn = \frac{x p_w}{D_B \left(\phi_w - \phi_\infty\right)} = -S'(0) \quad (18)$$

Here actual wall shear stress, heat flux (Fourier), solutal mass flux and nanoparticle mass flux are defined respectively as:

$$\tau_w = \mu_{tnf} u_y\Big|_0, \; q_w = -K_{tnf} T_y\Big|_0, J_w = -D_B C_y\Big|_0 \quad P_w = -D_B \phi_y\Big|_0 \quad (19)$$

3. MATLAB NUMERICAL PROCEDURE AND VALIDATION

Equations (9) to (12) with their accompanying boundary conditions (13) are first reduced to a system of first-order ordinary differential equations via suitable substitutions. This reduced system is then solved numerically using the MATLAB solver bvp4c which is a built-in numerical solver used to compute solutions for two-point boundary value problems (BVPs) for ordinary differential equations. It uses a finite difference code that implements a three-stage Lobatto IIIa formula, providing a fourth-order accurate continuous solution across your integration interval [22, 25]. The procedure is summarized in Fig. 2. Assuming:

$$\left.\begin{array}{l} F(\eta)=\Upsilon_1, G(\eta)=\Upsilon_4, H(\eta)=\Upsilon_6, S(\eta)=\Upsilon_8 \\ F'(\eta)=\Upsilon_2, G'(\eta)=\Upsilon_5, H'(\eta)=\Upsilon_7, S'(\eta)=\Upsilon_9 \\ F''(\eta)=\Upsilon_3, G''(\eta)=\Upsilon_5', H''(\eta)=\Upsilon_7', S''(\eta)=\Upsilon_9' \\ F'''(\eta)=\Upsilon_3' \end{array}\right\} \tag{20}$$

The following first-order differential equations are formulated from the original system of nonlinear differential equations giving:

$$\Upsilon_3' = -\frac{A_2}{A_1}\left((1+m)\Upsilon_1\Upsilon_3 - \Upsilon_2^{\,2} + Ri\left(\Upsilon_4 + Nc\Upsilon_6 - Nr\Upsilon_8\right)\cos(\gamma) - \frac{A_1}{A_2}K\Upsilon_2 - \frac{A_3}{A_2}\Upsilon_2 \right) \tag{21}$$

$$\Upsilon_5' = \frac{-\Pr A_5}{(A_4+R)}\left((1+m)\Upsilon_1\Upsilon_5 + Nb\Upsilon_9\Upsilon_5 + Nt\Upsilon_5^{\,2} + \frac{Q}{A_5}\Upsilon_4 \right) \tag{22}$$

$$\Upsilon_7' = -\left(Sc\Upsilon_1\Upsilon_7 - ScKr\left(1+\delta\Upsilon_1\Upsilon_4\right)^n \exp\left(-E/\left(1+\delta\Upsilon_1\Upsilon_4\right)\right)\right) \tag{23}$$

$$\Upsilon_9' = -\left(Le(1+m)\Upsilon_1\Upsilon_9 + \frac{Nt}{Nb}\Upsilon_5' \right) \tag{24}$$

$$\left.\begin{array}{l} \Upsilon_2 a = 1,\ \Upsilon_1 a = 0,\ \Upsilon_4 a = 1,\ \Upsilon_6 a = 1,\ \Upsilon_8 a = 1 \\ \Upsilon_2 b \to 0,\ \Upsilon_4 b \to 0,\ \Upsilon_6 b \to 0,\ \Upsilon_8 b \to 0 \end{array}\right\} \tag{25}$$

To validate the MATLAB bvp4c code, we benchmark against previous works. Husaain et al. [46] used a hyperbolic tangent nanofluid model to examine activation energy and viscosity on wedge geometries. Their results showed that increasing thermal and nanofluid Grashof numbers slows the fluid, while solutal Grashof number increases velocity. Hassanien et al. [47] studied power-law fluids over stretched sheets. Kulkarni [48] analysed binary chemical reactions in cone and wedge shapes using liquid hydrogen and found that increased activation energy and Schmidt numbers reduce mass diffusivity and lead to more efficient mass transfer.

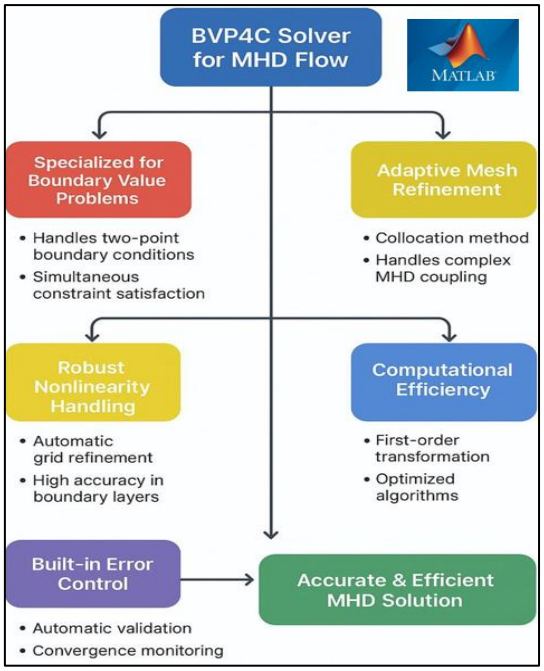


Fig. 2: MATLAB bvp4c solution methodology

Table 2 shows the current MATLAB solutions compared with all three quoted benchmark studies [46], [47], [48] for Nusselt number computed at different Pr with E=Nc=Nt=Nb=Nr=Ri=Sc=M=K=R=Q=Sc=Le=Kr=0. Excellent agreement is demonstrated and confidence in the present MATLAB code is therefore justifiably very high.

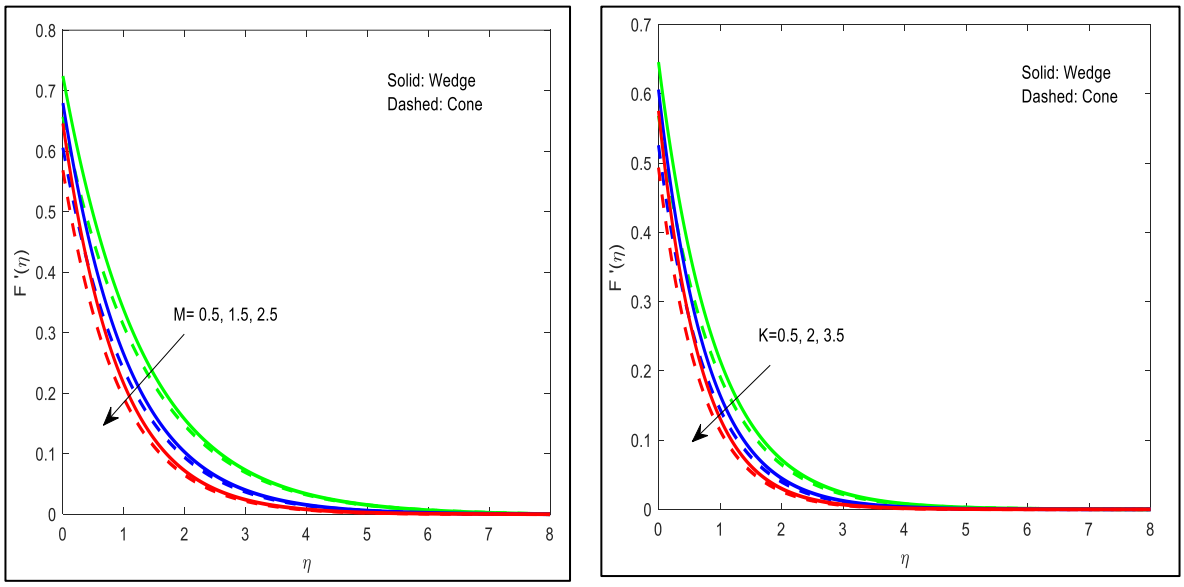
Table 2: Comparison of result for Nusselt number values of Pr with E=Nc=Nt=Nb=Nr=Ri=Sc=M=K=R=Q=Sc=Le=Kr=0.

Pr	MATLAB Solution	Kulkarni [48]	Hussain et al. [47]	Hassanien et al. [46]
0.72	0.46339	0.46342	0.46317	0.46325
1	0.58196	0.58198	0.58198	0.58198
3	1.16530	1.16526	1.16522	1.16525
5	1.56811	1.56809	1.56808	___
7	1.89546	1.89544	1.89548	___
10	2.30819	2.30812	2.30821	2.30801
100	7.76248	7.76252	7.76249	7.74495

4. MATLAB RESULTS AND DISCUSSION

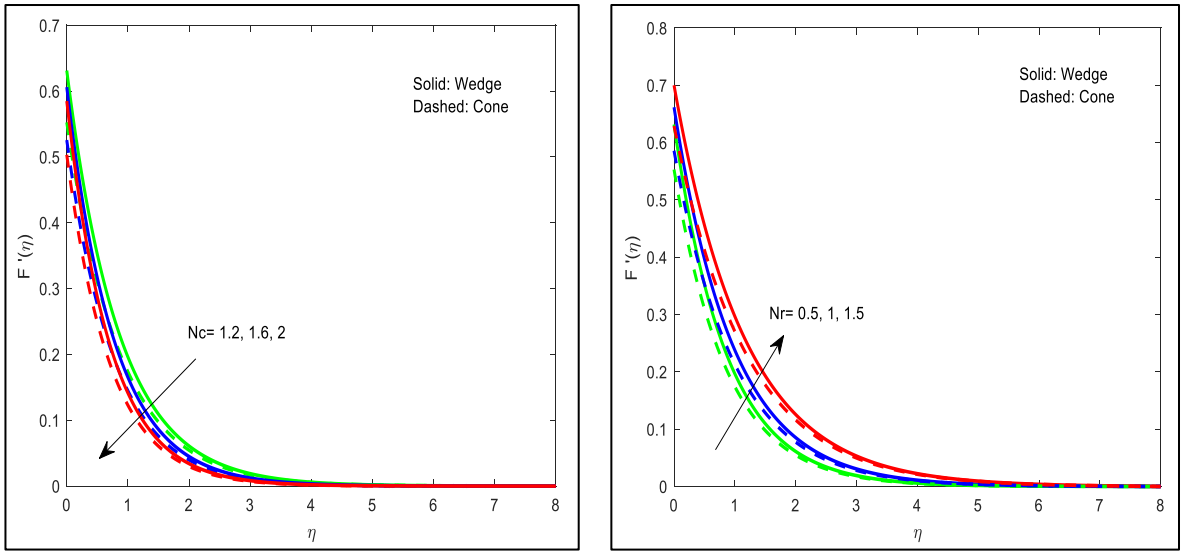
Figs. 3-9 depict the numerical solutions and illustrate the influence of different parameters e.g. radiation-conduction parameter, the Richardson number, the magnetic parameter, the

activation energy, and the permeability parameter on velocity F/(η), temperature $G(\eta)$, solute concentration $H(\eta)$, and nanoparticle volume fraction $S(\eta)$ for both wedge and cone cases.



(a) (b)

Figure 3: Influence (a) magnetic parameter (M) and (b) permeability parameter (K) on velocity.



(a) (b)

Figure 4: Influence (a) solutal buoyancy parameter (Nc) and (b) nanoparticle buoyancy parameter (Nr) on velocity.

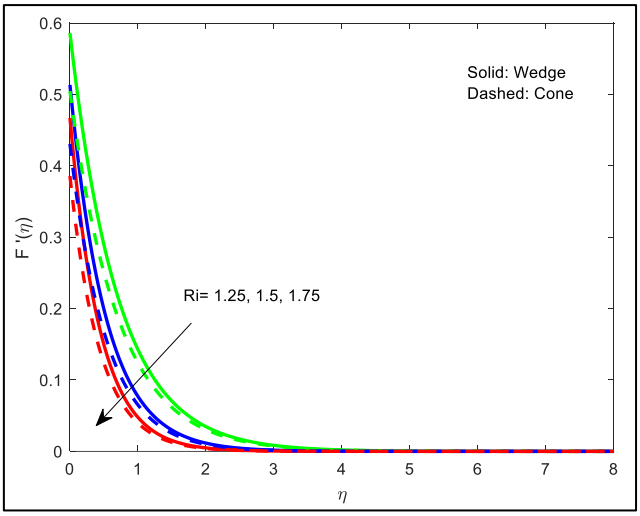
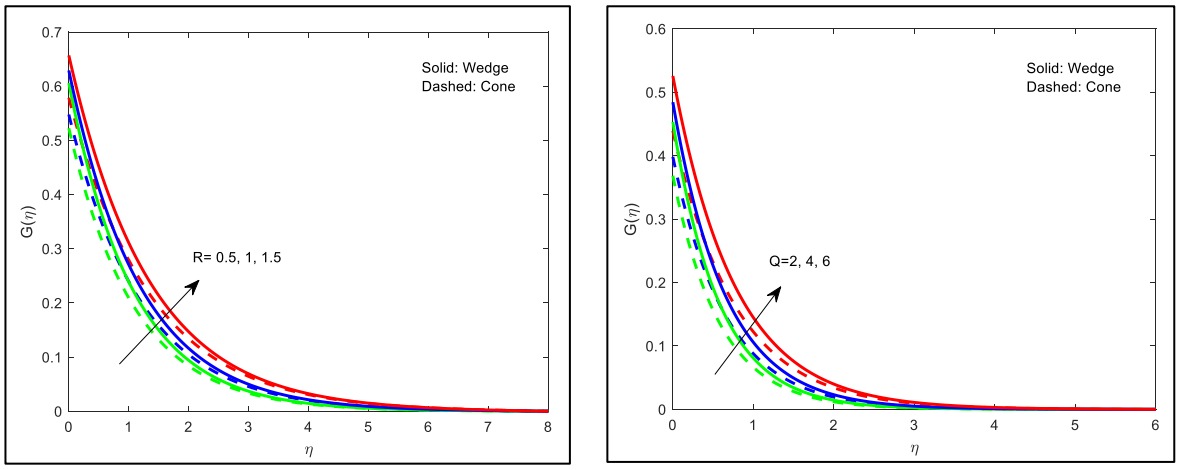
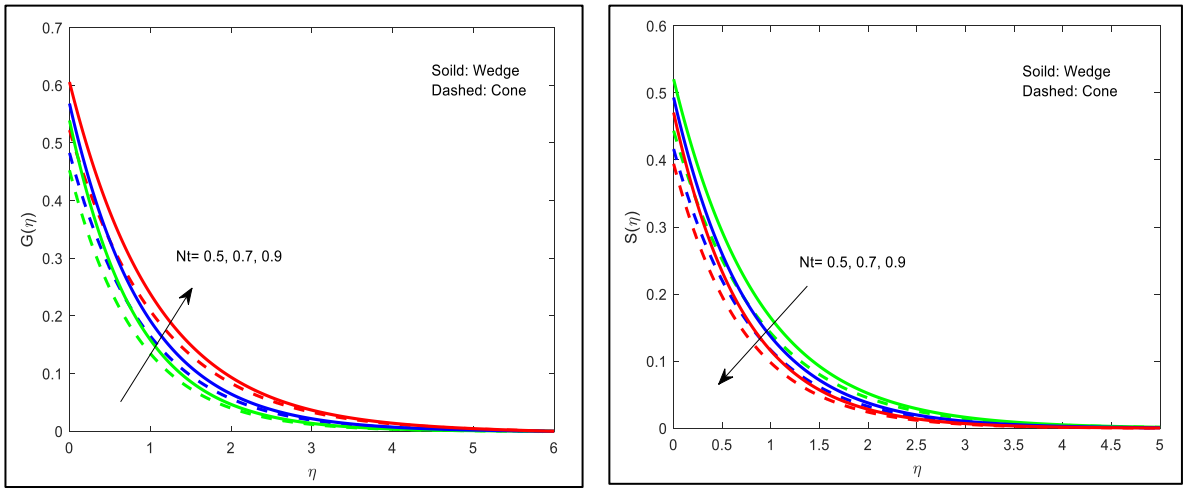


Figure 5: Influence of Richardson number (Ri) on velocity.



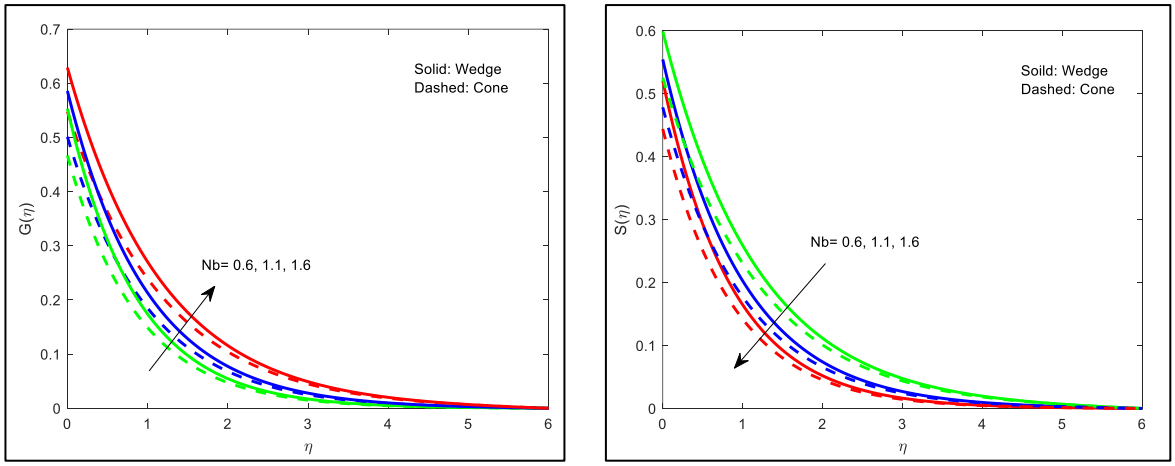
(a) (b)

Figure 6: Influence of (a) radiation-conduction parameter (R) and (b) heat source parameter (Q) on temperature.



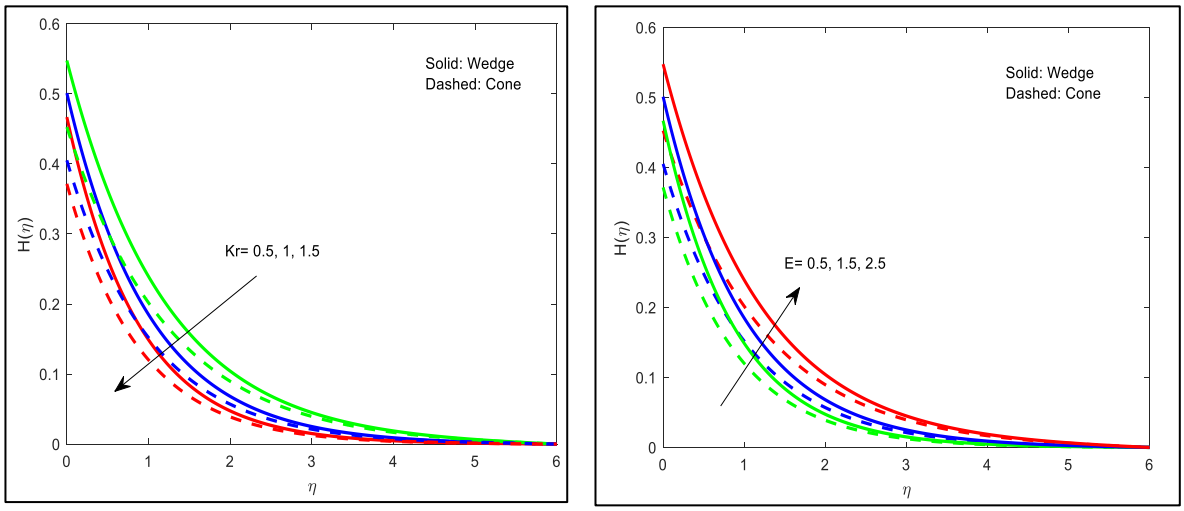
(a) (b)

Figure 7: Influence of thermophoresis parameter (Nt) (a) temperature and (b) nanoparticle concentration profiles.



(a) (b)

Figure 8: Influence of Brownian motion parameter (Nb) on (a) temperature and (b) nanoparticle concentration profiles.



(a) (b)

Figure 9: Influence of (a) chemical reaction parameter (Kr) and (b) activation energy (Ea) on solute concentration distributions.

Fig. 3 depicts the impact of (a) magnetic parameter (M) and (b) permeability parameter (K) on velocity. A strong damping is induced in the velocity field with increasing magnetic field strength in Fig. 3a. Slightly greater magnitudes of velocity are computed for the wedge compared with the cone. Asymptotically smooth decays are computed for the velocity field from the wall to the free stream confirming that convergence is achieved and the infinity boundary condition is adequately large in the MATLAB code. The magnetic parameter M is a modified Hartmann number which expresses the ratio of electromagnetic forces to viscous forces in the nanofluid. It is primarily used to understand how magnetic fields affect the flow of electrically conducting fluids. It features in the negative body force, $-\frac{A_3}{A_2}MF'(\eta)$ in the reduced momentum eqn. (9) which is linear. This is the Lorentz drag force associated with the magnetic field, which strongly counteracts the nanofluid motion. For both the wedge and the

cone, larger modified Hartmann magnetic number corresponds to progressively more intense magnetic field which decelerates the flow and increases momentum boundary layer thickness, although the cone produces a thicker momentum boundary layer. The impact of magnetic field is consistent at all locations transverse to the wedge/cone surface. Flow reversal is never induced, and velocity values remain positive. For M < 1, Lorentzian magnetic body force is dominated by viscous hydrodynamic force and at M = 0.5 maximum velocity is computed. However, for M > 1, Lorentzian force exceeds the viscous force and at M = 2.5 (strongest magnetic field case), minimal velocity is computed. In coating processes, magnetic field can therefore be exploited as a non-intrusive mechanism for regulating the flow velocity, coating thickness, and particle alignment. Magnetic fields cause nanoparticles to align and form chain-like structures. This temporarily increases the nanofluid effective viscosity, which resists levelling and can impact the smoothness of the final coating. Engineers can therefore fine-tune the Lorentz force orienting the suspended magnetic particles, creating directional structural properties as the coating cures [6]. Fig. 3b displays the influence of the permeability parameter, K on velocity evolution. K is directly related to actual porous medium permeability and features in the Darcian drag force, $-\frac{A_1}{A_2}KF'(\eta)$ in the momentum boundary layer eqn. (9). As K is increased, actual permeability is reduced which implies an increase in quantity of solid fibers. The nanofluid percolation is suppressed in the less permeable medium and this accentuates the Darcian drag leading to strong flow deceleration. Porous media fibers influence coating flow by altering fluid hydrodynamics at the substrate interface, inducing pressure gradients, and driving liquid penetration. The fiber matrix creates capillary suction, affects the apparent viscosity of the coating, and limits the thickness of the entrained film. In modern coating systems, nanofluid flow through flexible fibrous structures can cause the fibers themselves to bend, compress, or realign, which actively changes the local permeability and flow pathways. However, this requires a more sophisticated porous medium model which is beyond the scope of the present work but is being considered for future simulations. It is again noteworthy that the wedge produces marginally greater velocity magnitudes than the cone. A wedge restricts flow to two dimensions, meaning fluid displaced by the coating substrate can only move in a restricted fashion. For the cone, improved lateral spreading is possible which enables the coating nanofluid to diverge sideways and lose more kinetic energy producing stronger deceleration and a thicker hydrodynamic boundary layer. The lack of lateral spreading in a wedge generally imposes a stronger compression and a steeper favourable pressure gradient in

the direction of motion, which acts to accelerate the fluid locally and produces a thinner momentum boundary layer than for a cone.

Fig. 4a, b visualizes the influence of a) solutal buoyancy (Nc) and (b) nanoparticle species buoyancy parameter (Nr) on velocity profiles. Both parameters feature in the term, $+Ri\big(G(\eta)+NcH(\eta)-NrS(\eta)\big)\,cos(\gamma)$ in eqn. (9). In Fig. 4b, as Nc is elevated there is a strong damping in velocity i.e. flow retardation is induced and momentum boundary layer thickness of the nanofluid coating is increased. $Nc=\frac{\beta_c(C_w-C_\infty)}{\beta_t(T_w-T_\infty)}$ and expresses the ratio of the solute buoyancy force to the thermal buoyancy force. In anti-corrosion nano-coatings, the solute is often oxygen, hydrogen or may be an organic molecule (e.g., acetic acid or toluene). Mass transfer is driven by solubility and sorption parameters of the solute within the nano-coating matrix. For Nc > 1 as examined here in Fig. 4a, the solutal buoyancy force dominates the thermal buoyancy force (natural convection). When combined with thermal buoyancy (thermo-solutal convection), the relative strength and direction of solutal buoyancy dictate whether it will assist or oppose the overall flow. Clearly stronger solutal buoyancy mitigates momentum diffusion and decreases velocity magnitudes. It also interacts with Brownian motion and thermophoresis to prevent nanoparticle agglomeration. This hydrodynamic stability promotes a more uniform distribution of micro-nano structures on the substrate. Again, larger velocity magnitudes are associated with wedge geometry compared with the cone geometry at all locations. Fig. 4b shows that the opposite trend is computed with increment in nanoparticle species buoyancy parameter (Nr). This parameter is defined as $Nr=\frac{(\rho-\rho_f)(\phi_w-\phi_\infty)}{\rho_f\beta_t(T_w-T_\infty)(1-\phi_\infty)}$ and produces an acceleration effect in the nanocoating boundary layer. For Nr = 1 both nanoparticle buoyancy force and thermal buoyancy force are equivalent. However, for Nr > 1, as considered here, nanoparticle buoyancy force exceeds the thermal buoyancy force. This dominant buoyancy increases fluid velocity near the coating interface, continually renewing the concentration boundary layer and increasing the nanoparticle deposition rate. The nanoparticle species buoyancy force is modulated by fluid motion driven by density variations from nanoparticle concentration gradients. It accelerates nanocoating mass transfer by inducing natural convection. As nanoparticles diffuse, they alter local fluid density, creating buoyant forces that agitate the fluid, enhance mixing, and transport functional materials more efficiently toward the coating surface. Again, greater velocity is observed for the wedge relative to the cone i.e. thinner hydrodynamic boundary layers are associated with the wedge geometry. Effectively the increased upward force caused by the density difference between the base fluid

and the nanoparticles causes the fluid velocity to be elevated in both wedge and cone geometries. Momentum diffusion is assisted in both cases, although it is more dramatic for the wedge case.

Fig. 5 depicts the impact of Richardson number on velocity distribution. Richardson number (Ri) dictates the balance between buoyancy-driven (natural) convection and shear-driven (forced) convection. In nanocoating flows (e.g. enrobing), Ri determines whether the coating liquid spreads via mechanical inertia or thermal/solutal buoyancy, directly impacting layer uniformity and nanoparticle distribution. Ri = Gr/Re2 and features explicitly in the hydrodynamic boundary layer eqn. (9) i.e. in the terms $Ri\big(G(\eta) + NcH(\eta) - NrS(\eta)\big)\,cos(\gamma)$. In Fig. 5a, b we consider scenarios wherein Ri > 1. For Ri <1 (not examined), forced convection dominates. Inertial forces and shear from the substrate speed completely override buoyancy. The flow is smooth and predictable, driven purely by mechanical movement. However, this range of Richardson number is only ideal for thin-film uniformities (e.g., spin coating). However, if shear rates are too high, they can cause flow-induced defects or particle alignment. In enrobing coating flows, as considered here, Ri > 1 and thermal buoyancy force therefore dominates. Temperature or density differences (due to nanoparticle concentration gradients or evaporation cooling) generate strong natural convection currents, and this suppresses the velocity field and produces enhanced control of the coating enabling homogeneity to be achieved in surface finishing. Momentum boundary layer thickness is therefore increased with larger Richardson number. It is also pertinent to mention that for the intermediate case Re ~1, again not plotted here, the thermal buoyancy and mechanical shear are evenly matched. However, in practical nano-coating operations, the flow structures are rendered very complex. Nanoparticles are subject to both forced advection and thermally driven thermophoresis (particle migration due to temperature gradients). This can produce cause undesirable variations in coating thickness if the thermal environment is unstable. However, engineers may be able to actively tune Ri ≈ 1 in heated chambers to intentionally create specific, self-assembling nanoparticle patterns, although this is very expensive [6].

Figure 6a, b visualizes the distribution of temperature, G (η) for various values of (a) radiation-conduction parameter (R) and (b) heat source parameter (Q). An upward trend in the temperature is observed with increment in R. Higher temperatures correspond to the wedge case relative to the cone case. Higher radiative heat flux thickens the thermal boundary layer but reduces the momentum boundary layer, impacting how the coating spreads and levels out

on a substrate (i.e. cone or wedge surface). The Rosseland radiative flux model augments thermal conductivity in the term $\frac{(A_4+R)}{A_5}G''(\eta)$ in the heat eqn. (10). It therefore simplifies radiative heat transfer for optically thick nano-coatings [6] by treating radiation as a diffusion process. Instead of calculating complex photon paths, it adds a radiative conductivity to the standard thermal conductivity, bypassing the need to solve computationally expensive transport equations. The parameter, $R = \frac{16\sigma^* T_\infty^3}{3k^* k_f}$ expresses the relative contribution of thermal radiation heat transfer to thermal conduction heat transfer. It is also known as Stark number or Boltzmann number in thermal fluid dynamics. When R = 0 radiative heat flux vanishes. For R = 1, both thermal radiation and conduction contribute equally. For R > 1, radiative heat dominates. Thermal radiation increases the temperature of the nanocoating, which boosts fluid velocity and modifies the thickness of the thermal boundary layer. This effect depends on both the radiative heat flux intensity and nanoparticle volume fraction. These interactions govern how heat diffuses during drying and curing processes. Rosseland's model correctly predicts the energization of the nano-coating and temperature boost. However, it does have limitations. It cannot account for scattering effects in a medium. It also lacks directional capability since it assumes isotropic radiation propagation and therefore cannot accommodate highly directional radiation fluxes. Alternative radiative transfer models such as Chandrasekhar's discrete ordinates method (DOM) and the P1 approximation are more accurate but computationally expensive. Fig. 6b indicates that increasing heat generation (source) i.e. Q also strongly accentuates temperature magnitudes. Higher magnitudes again correspond to the wedge case compared with the cone case. A faster rate of temperature decay from the substrate surface accompanies the cone case. The presence of a heat source i.e. the term, $+\frac{Q}{A_5}G(\eta)$ in eqn. (10), dictates the phase state, velocity, and thermal degradation of nanomaterials. Nanocoating manufacturing utilizes several heat sources depending on the specific deposition and curing requirements. For thermal spray, physical vapor deposition, and curing of nanocomposite films, manufacturers commonly rely on high-energy lasers, thermal plasmas, and microwave or infrared radiation to achieve nanometer-scale precision and structural uniformity [6].

Fig. 7a, b illustrates the response in (a) temperature and (b) nanoparticle concentration profiles to variation in thermophoresis parameter (Nt). In both the wedge and cone scenarios, Nt significantly affects both temperature and nanoparticle concentration, but the influence is different. Thermophoresis is the migration of nanoparticles in response to a temperature gradient. Its overall effect is the creation of a steady-state concentration gradient that alters the

local concentration of the nanoparticles across the system. Nanoparticles may be thermophobic or thermophilic. Thermophobic nanoparticles migrates from the hot region to the cold region which produces a depletion in the hot area and an accumulation of solute in the cold area. This elevates thermal diffusion and boosts temperatures as observed in Fig. 7a. In nanofluid coatings, the thermophoretic body force combined with Brownian motion drives the targeted delivery of nanoparticles. This regulates thermal resistance and enhances heat transfer efficiency, significantly improving the performance of the nanocoating. This mobilization depletes the concentration of nanoparticles, $S(\eta)$ and produces a thinner nanoparticle species boundary layer as observed in Fig. 7b. Thicker thermal boundary layers are produced with higher values of Nt. It is also noteworthy that thermophilic nanoparticles (not considered here) biomolecules in certain buffers) move from the cold region to the hot region. This results in a net nanoparticle concentration increase in the hotter areas.

Fig. 8a, b displays the evolution in (a) temperature and (b) nanoparticle concentration profiles with modification in Brownian motion parameter (Nb). In nanofluid coatings, Brownian motion drives the random, zig-zag movement of nanoparticles within the liquid base. This nanoscale convection enhances heat transfer, promotes uniform particle dispersion, and prevents rapid settling before curing. However, excessive motion can lead to nanoparticle agglomeration, altering the coating's structural and thermal properties. The erratic jiggling of the nanoparticles which are smaller than 100 nm in dimension, creates micro-convection currents in the base fluid, increasing the overall thermal conductivity. This manifests in an escalation in temperature and associated thermal boundary layer thickness, as shown in Fig. 8a. The rapid energy exchange allows for a more uniform temperature distribution across the coated surface. Brownian motion is therefore extremely beneficial for intensifying heat diffusion in nano-coatings and produces higher temperatures for the wedge case. Fig. 8b shows that increasing Brownian motion parameter suppresses the nanoparticle volume fraction (concentration). Brownian motion causes nanoparticles to constantly jitter and disperse throughout a liquid coating. This random motion counteracts gravity, preventing rapid settling and maintaining a more uniform nanoparticle volume fraction. However, over time, this diffusion causes particles to migrate toward areas of lower concentration, altering the coating's structural properties. The volume fraction of nanoparticles (the ratio of nanoparticle volume to the total volume of the coating matrix) is heavily governed by particle-to-particle dynamics and their interaction with the surrounding base fluid. Continuous collisions with fast-moving solute molecules generate random, erratic movements (Brownian motion). This process

provides a natural repulsive force that keeps nanoparticles suspended. According to Fick's laws of diffusion, this random jitter naturally drives nanoparticles away from dense clumps and toward regions of lower concentration. This ensures the volume fraction remains homogeneous during the wet phase. If Brownian motion is weak i.e. Nb <<1 (e.g., particles are too large or the suspension is unstable), Van der Waals attractive forces dominate, causing the nanoparticles to cluster together. When clustering occurs, the effective local volume fraction drops as particles fall out of suspension, leading to poor scratch resistance and uneven coloration. In the Buongiorno model larger Nb implies smaller nanoparticle dimensions and vice versa. A higher nanoparticle volume fraction generally increases the viscosity of liquid coatings. Strong Brownian motion helps mitigate extreme viscosity spikes by keeping the particles efficiently spaced apart. If the volume fraction becomes too high, the Brownian motion is restricted, which can result in a brittle or poorly levelled dry coating.

Fig. 9a, b displays the impact of (a) chemical reaction parameter (Kr) and (b) activation energy (Ea) on solute concentration distributions, H (η). Both chemical parameters feature in the term, $-ScKr\left(1+\delta G(\eta)\right)^{n} exp\left(-E/\left(1+\delta G(\eta)\right)\right)$ in the solute concentration boundary layer eqn. (11). Figure 9a clearly demonstrates that solute concentration diminishes as the chemical reaction parameter has been increased. Since a homogenous destruction chemical reaction is taking place in the nanofluids, more solute is consumed and this produces a depletion in concentration magnitudes. Solute species boundary layer thickness is therefore also reduced. Higher solute concentration magnitudes are produced for the wedge geometry and slightly lower values for the cone geometry. Figure 9b shows the concentration curves for various activation energy E values. Assigning the maximum value to E results in the solute concentration reaching its maximum level. Activation energy is the minimum energy required for a chemical reaction to occur. It acts as a barrier that reactants must overcome to transform into products, often involving the formation of a transition state or an intermediate structure that is higher in energy than the reactants. This energy can vary significantly between different reactions and is crucial in determining reaction rates, as described by the Arrhenius equation. In processes like thermal curing or nano-coating deposition, a high activation energy means the reaction is highly sensitive to temperature. If the temperature drops or activation energy is too high, the activation barrier is not overcome, stalling the coating formation and dropping the mass transfer rate. In diffusion-controlled coating (low activation energy), such as drying processes, the barrier for reactant molecules to move through the already-coated layer dictates the speed. When the activation energy for diffusion is low, coating molecules can

transport rapidly to the surface without relying heavily on extreme temperature increases. An increase in activation energy generally imposes a stronger energetic barrier that suppresses mass diffusion and therefore reactants fail to diffuse as deeply into the substrate, slowing the reaction and causing an accumulation (or higher concentration) of unreacted species near the coating surface, and a concomitant decrease in solute concentration across the boundary layer, as observed in Fig. 9b. Managing activation energy is crucial for optimizing manufacturing line speeds, minimizing defects, and controlling film thickness. Engineers typically manipulate the coating formulation or ambient conditions to balance the mass transfer barrier: Increasing the ambient or substrate temperature exponentially increases the kinetic energy of the molecules. This ensures a greater fraction of molecules can overcome the activation energy barrier, thus accelerating the coating mass flux to the wall and curing rates, but lower solutal concentration boundary layer thickness. It is noteworthy that in nanocoating synthesis, adding catalysts effectively lowers the activation energy of the curing reaction. This allows high-quality cross-linking to occur at much lower temperatures or at much faster speeds on a production line.

5. RESPONSE SURFACE METHODOLOGY (RSM)

Having established a robust numerical solution to the nanocoating transport problem in section 4, here we examine the sensitivity of the model to different multi-physical parameters. Response Surface Methodology (RSM) is an excellent tool for studying processes with multiple variables. It furnishes insight into the input components that have different degrees of impact on the results. By mapping how independent variables (e.g. magnetic field intensity) affect a response (e.g., Nusselt number), RSM identifies optimal operating conditions without requiring exhaustive, full-scale experimental or numerical testing. It has been successfully deployed in recent years in multiple thermal fluid dynamics applications including magnetic nanofluid fuel cell porous media enclosure flows [50, 51], nanofluid tribological squeezing [52], thermo-magnetic viscoplastic Casson hybrid nanofluid bilinear stretching with Joule magnetic dissipation [53] and Sisko non-Newtonian hybrid nanofluid transport from biaxial stretching surfaces in porous media [54]. RSM is therefore very versatile and is implemented in the present study to explore how different input factors. We examine for both wedge and cone geometries:

(i)The influence of M, K, and Nc on skin friction.

(ii)The impact of R, Q, and Nt on Nusselt number influences,

(iii) The effect of Kr, E, and Sc on solute Sherwood number.

(iv)The consequence of Nt, Nb, and E on nanoparticle Sherwood number.

As shown in Tables 3, 6, 9, and 12, input parameters were adjusted within specified ranges, with three levels being evaluated for each. Tables 4, 7, 10, and 13 demonstrate the generation and execution of the statistical model 20 times after selecting the input parameters. A second-order polynomial is used to simulate the interaction effects of the response and input variables. This model is constructed using a second-order polynomial, where J0 denotes the intercept, Ji the linear coefficients, Jii the quadratic coefficients, and Jij the interaction coefficients. Regression coefficients, which measure the connections between the input parameters, alter these terms. To fit the polynomial and measure these connections, Central Composite Design (CCD) is employed. CCD is the most widely used experimental design for mapping and optimizing complex, non-linear processes. It allows engineers to build a comprehensive quadratic model using significantly fewer experimental runs than a full three-level factorial design. CCD successfully captures the main effects, interactions, and quadratic (curved) responses necessary to identify the true optimal settings for a process. CCDs are typically constructed to be rotatable, meaning the precision of the predicted response remains constant at all points equidistant from the centre of the design space as elaborated by Anderson and Whitcomb [55]. For a total of twenty separate trials, this layout includes 6 axial points, 8 cube points, and 6 centre points. Its design improves factor space exploration and allows for efficient regression coefficient estimation [50-55].

5.1 Influence of M, K and Nc on skin friction (Cf).

Table 3: Effects of varying Skin friction parameters.

Parameter	Symbol	Level		
		-1	0	1
$0.5 \le M \le 2.5$	W1	0.5	1.5	2.5
$0.5 \le K \le 3.5$	W2	0.5	2	3.5
$1.2 \le Nc \le 2$	W3	1.2	1.6	2

The skin friction correlation used is:

$$Cf = J_0 + J_1 M + J_2 K + J_3 Nc + J_{11} M^2 + J_{22} K^2 + J_{33} Nc^2 + J_{12} M * K + J_{13} M * Nc + J_{14} K * Nc \quad (26)$$

The ANOVA is used to ensure that the suggested model is both appropriate and effective. According to the results in Table 5, parameters that have p-values below 0.05 are considered to possess statistical significance, whilst those with greater p-values are considered non-significant.

Table 4: CCD approach for skin friction (Cf)

Run	Code values			Real values			Response	
	W1	W2	W3	*M*	*K*	*Nc*	Cf / Wedge	Cf / Cone
1	-1	-1	1	0.5	0.5	2	0.372822	6.11998
2	-1	0	0	0.5	2	1.6	4.13431	4.36525
3	0	0	0	1.5	2	1.6	8.37435	15.4817
4	-1	-1	-1	0.5	0.5	1.2	6.96685	5.71708
5	0	0	0	1.5	2	1.6	8.37435	15.4817
6	0	0	0	1.5	2	1.6	8.37435	15.4817
7	0	-1	0	1.5	0.5	1.6	4.15668	4.23505
8	1	-1	1	2.5	0.5	2	41.7006	12.8021
9	1	-1	-1	2.5	0.5	1.2	0.117422	8.52675
10	1	0	0	2.5	2	1.6	12.8807	24.4266
11	1	1	1	2.5	3.5	2	9.40541	8.82613
12	0	0	-1	1.5	2	1.2	7.55869	9.43011
13	0	0	0	1.5	2	1.6	8.37435	15.4817
14	1	1	-1	2.5	3.5	1.2	5.18991	8.6701
15	0	0	0	1.5	2	1.6	8.37435	15.4817
16	-1	1	1	0.5	3.5	2	1.58913	8.25167
17	-1	1	-1	0.5	3.5	1.2	7.15968	10.8121
18	0	0	1	1.5	2	2	2.64396	6.62527
19	0	1	0	1.5	3.5	1.6	4.07712	15.2103
20	0	0	0	1.5	2	1.6	8.37435	15.4817

In the wedge configuration, Nc, M2 and K2 are not significant, and in the cone configuration, K, M2, and the interaction term M*K have no major impact. The model is highly accurate, with coefficient of determination (R2) values of 99.73% for the wedge and 98.45% for the cone. The findings show a clear link among the input parameters M, K, and Nc and the skin friction values, as follows:

$$Cf(wedge) = 7.20 + 4.91M - 2.59K - 0.33Nc^2 - 3.58M * K + 7.25M * Nc - 4.54K * Nc \quad (27)$$

$$Cf(cone) = 14.39 + 2.80M - 0.05Nc - 3.02K^2 - 4.71Nc^2 + 0.82M * Nc - 0.89K * Nc \quad (28)$$

Table 5: Analysis of Variance (ANOVA) of Cf .

Source	DF	Adjusted SS		Adjusted MS		F-value		p-value		Coefficient	
		Wedge	Cone	Wedge	Cone	Wedge	Cone	Wedge	Cone	Wedge	Cone
Model	9	1106.54	305.087	122.949	33.8986	14.09	11.68	0.019	0.014	-	-
Linear	3	390.32	98.995	130.108	32.9985	13.33	9.64	0.034	0.042	7.20	14.39
M	1	240.80	78.319	240.799	78.3194	18.01	33.89	0.018	0.007	4.91	2.80
K	1	67.05	20.648	67.045	20.6478	20.23	1.03	0.016	0.335	-2.59	1.44
Nc	1	82.48	0.028	82.480	0.0282	2.74	11.00	0.129	0.007	2.87	-0.05
Square	3	28.66	179.106	9.554	59.7021	0.32	2.97	0.812	0.004	-	-
M*M	1	25.98	7.518	25.976	7.5182	0.86	0.37	0.375	0.555	3.07	1.65
K*K	1	4.77	25.078	4.771	25.0779	0.16	19.25	0.699	0.020	-1.32	-3.02
Nc*Nc	1	0.30	61.130	0.305	61.1305	0.01	13.04	0.922	0.012	-0.33	-4.71
2-way interaction	3	687.55	26.986	229.184	8.9953	7.62	0.45	0.006	0.725	-	-
M*K	1	102.47	15.289	102.473	15.2886	23.41	0.76	0.005	0.404	-3.58	-1.38
M*Nc	1	419.97	5.427	419.967	5.4267	13.96	9.27	0.004	0.015	7.25	0.82
K*Nc	1	165.11	6.270	165.113	6.2705	5.49	10.31	0.041	0.029	-4.54	-0.89
Error	10	300.73	201.259	30.073	20.1259						
Lack-of-Fit	5	300.73	201.259	60.146		*	*	*	*		
Pure Error	5	0.000	0.00	0.000	0.0000						
Total	19	1407.27	506.346								

Figs. 10 and 11 provide respectively the difference between residual and observation for Cf for the wedge and the cone.

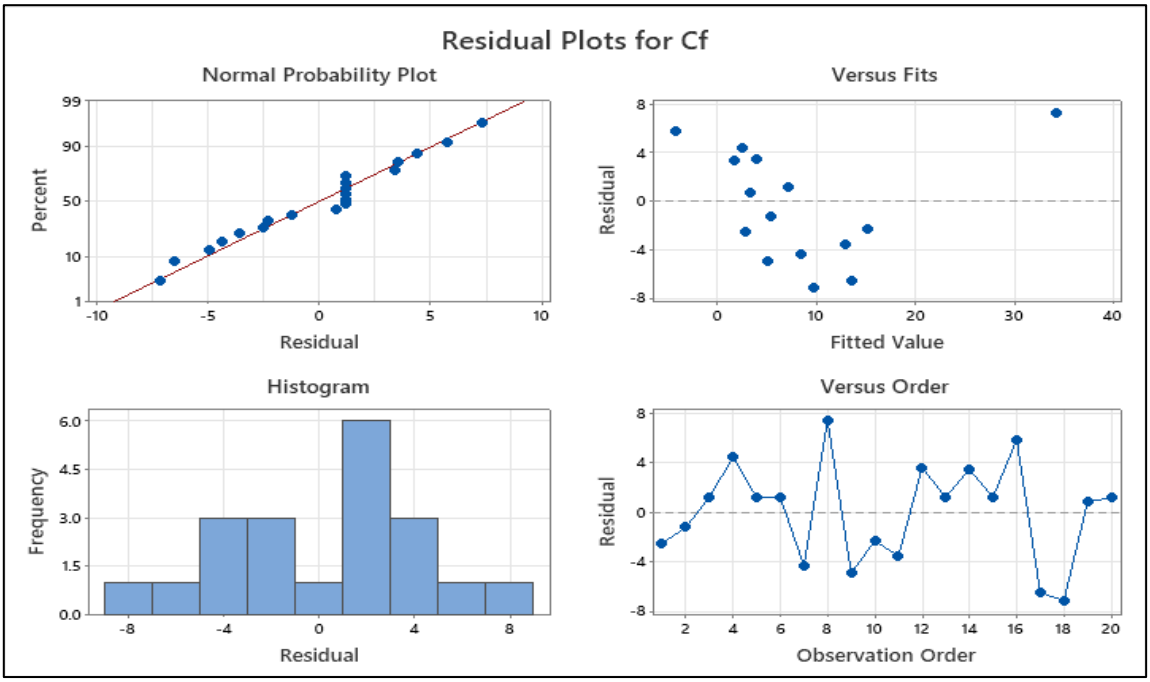


Figure 10: The difference between residual and observation for Cf $(wedge)$.

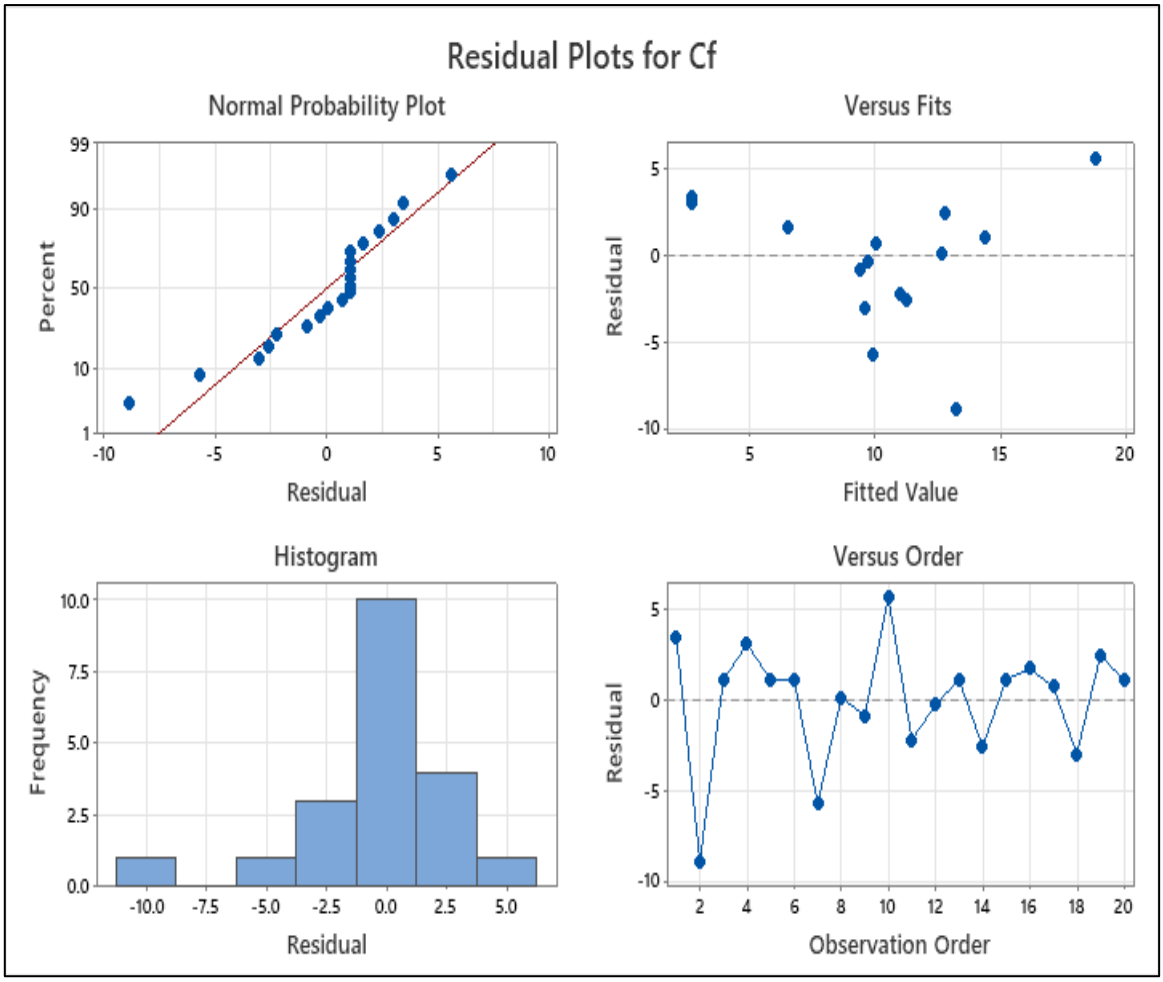


Figure 11: The difference between residual and observation for $Cf\,(cone)$.

5.2 Influence of R, Q and Nt on Nusselt number (Nu)

Next, we consider the Nusselt number, Nu.

Table 6: The impact of different parameter values for Nusselt number.

Parameter	Symbol	Level		
		-1	0	1
$0.5 \le R \le 1.5$	W1	0.5	1	1.5
$2 \le Q \le 6$	W2	2	4	6
$0.5 \le Nt \le 0.9$	W3	0.5	0.7	0.9

The Nusselt number correlation used is:

$$Nu = J_0 + J_1 R + J_2 Q + J_3 Nt + J_{11} R^2 + J_{22} Q^2 + J_{33} Nt^2 + J_{12} R*Q + J_{13} R*Nt + J_{14} Q*Nt \quad (29)$$

Table 7: An approach to research grounded upon CCD.

Run	Code values			Real values			Response	
	W1	W2	W3	*R*	*Q*	*Nt*	*Nu* / Wedge	*Nu* / Cone
1	-1	-1	1	1	4	0.9	1.57548	1.79307
2	-1	0	0	1.5	6	0.5	3.04686	0.830585
3	0	0	0	1	4	0.7	1.57042	1.85335
4	-1	-1	-1	1.5	2	0.9	1.56352	4.19221
5	0	0	0	1	4	0.7	1.57042	1.85335
6	0	0	0	1	4	0.7	1.57042	1.85335
7	0	-1	0	1	4	0.7	1.57042	1.85335
8	1	-1	1	1.5	6	0.9	0.0654954	2.565
9	1	-1	-1	1.5	2	0.5	1.56015	2.89134
10	1	0	0	0.5	6	0.5	4.46344	2.3688
11	1	1	1	1	2	0.7	1.57121	3.48555
12	0	0	-1	1	4	0.7	1.57042	1.85335
13	0	0	0	1	6	0.7	3.61383	2.62172
14	1	1	-1	1.5	4	0.7	1.56135	2.02408
15	0	0	0	0.5	2	0.9	1.58168	3.47373
16	-1	1	1	1	4	0.7	1.57042	1.85335
17	-1	1	-1	0.5	6	0.9	5.58098	3.00723
18	0	0	1	0.5	2	0.5	1.58042	3.14851
19	0	1	0	1	4	0.5	10.4168	1.95573
20	0	0	0	0.5	4	0.7	1.99998	1.55538

The ANOVA is used to confirm the model's validity and practical applicability, with the results shown in Table 8. Parameters that have p-values below 0.05 are considered to have statistical significance. In the wedge case, R2 and Q*Nt are non-significant and in the cone case, R, R2, and Nt2 are not statistically significant. The model is very reliable, with coefficients of determination (R2) of 99.85% for the wedge and 97.65% for the cone. The data analysis shows a strong connection between the input parameters R, Q and Nt and the Nusselt number values, as follows:

$$Nu(wedge) = 2.268 - 0.741R + 0.891Q - 1.07Nt - 0.72Q^2 + 2.68Nt^2 - 0.862R*Q - 0.512R*Nt \quad (30)$$

$$Nu(cone) = 1.883 - 0.5798Q + 0.3836Nt + 1.127Q^2 - 0.305R*Q + 0.259R*Nt + 0.093Q*Nt \quad (31)$$

Table 8: Analysis of Variance (ANOVA) of Nu.

Source	DF	Adjusted SS		Adjusted MS		F-value		p-value		Coefficient	
		Wedge	Cone	Wedge	Cone	Wedge	Cone	Wedge	Cone	Wedge	Cone
Model	9	54.0271	11.5182	6.0030	1.27980	1.47	14.18	0.279	0.000	-	-
Linear	3	24.8849	4.9437	8.2950	1.64791	18.03	18.26	0.017	0.000	2.268	1.883
R	1	5.4895	0.1103	5.4895	0.11034	11.34	1.22	0.024	0.295	-0.741	-0.105
Q	1	7.9453	3.3617	7.9453	3.36169	10.94	37.24	0.014	0.000	0.891	-0.5798
Nt	1	11.4501	1.4717	11.4501	1.47170	12.80	16.30	0.025	0.002	-1.070	0.3836
Square	3	20.6676	5.2230	6.8892	1.74101	1.68	19.29	0.233	0.000	-	-
R*R	1	6.4758	0.0515	6.4758	0.05150	1.58	0.57	0.237	0.467	-1.53	-0.137
Q*Q	1	1.4363	3.4932	1.4363	3.49318	14.35	38.70	0.007	0.000	-0.72	1.127
Nt*Nt	1	19.7653	0.0075	19.7653	0.00749	14.83	0.08	0.003	0.779	2.68	-0.052
2-Way Interaction	3	8.4746	1.3514	2.8249	0.45048	0.69	4.99	0.579	0.023	-	-
R*Q	1	5.9403	0.7453	5.9403	0.74527	16.45	8.26	0.026	0.017	-0.862	-0.305
R*Nt	1	2.0980	0.5365	2.0980	0.53646	7.51	5.94	0.049	0.035	-0.512	0.259
Q*Nt	1	0.4364	0.0697	0.4364	0.06971	0.11	8.77	0.751	0.040	-0.234	0.093
Error	10	40.9373	0.9026	4.0937	0.09026						

Lack-of-Fit	5	40.9373	0.9026	8.1875	0.18052	*	*	*	*		
Pure Error	5	0.0000	0.0000	0.0000	0.0000						
Total	19	94.9643	12.4208								

Figures 12, 13 document the difference between residual and observation for Nu $(wedge)$ and Nu $(cone)$.

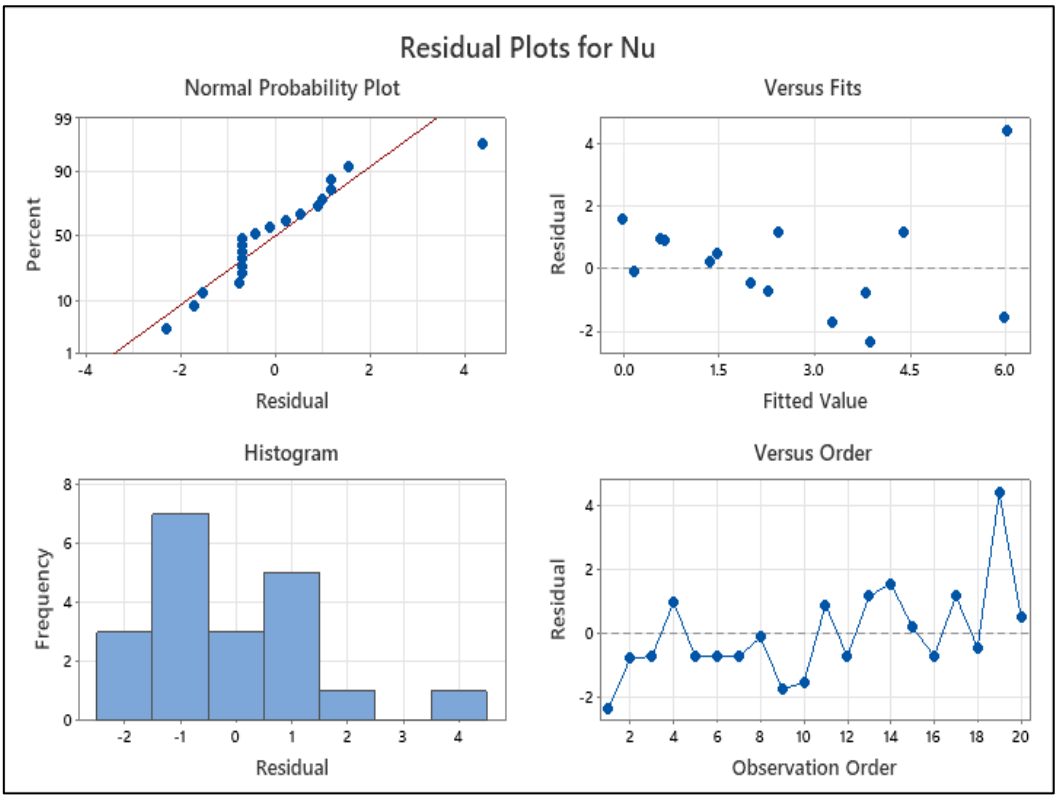


Figure 12: The difference between residual and observation for Nu $(wedge)$.

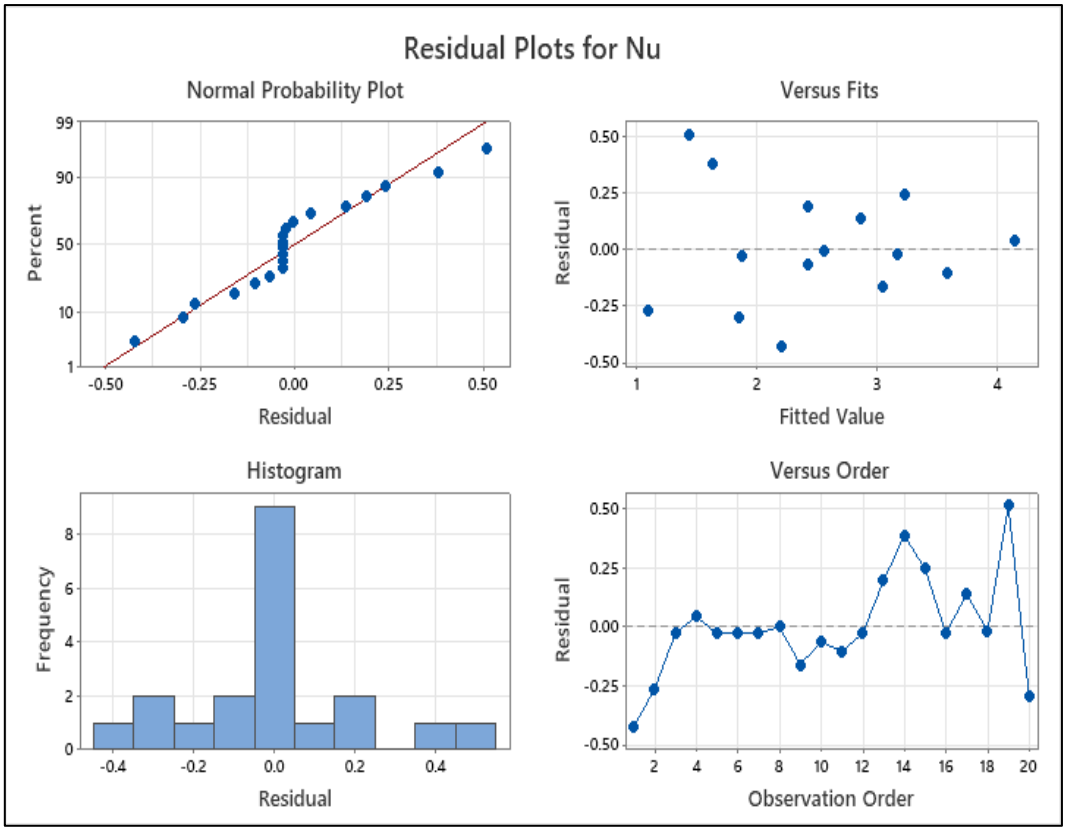


Figure 13: The difference between residual and observation for Nu $(cone)$.

5.3 Influence of Kr, E and Sc on solutal Sherwood number (Sh)

Now we address solutal Sherwood number (Sh).

Table 9: The impact of different parameter values for Sherwood number.

Parameter	Symbol	Level		
		-1	0	1
$0.5 \le Kr \le 1.5$	W1	0.5	1	1.5
$0.5 \le E \le 2.5$	W2	0.5	1.5	2.5
$0.6 \le Sc \le 0.8$	W3	0.6	0.7	0.8

The solutal Sherwood number (Sh) correlation adopted is:

$$Sh = J_0 + J_1 Kr + J_2 E + J_3 Sc + J_{11} Kr^2 + J_{22} E^2 + J_{33} Sc^2 + J_{12} Kr * E + J_{13} Kr * Sc + J_{14} E * Sc \quad (32)$$

Table 10: An approach to research grounded upon CCD.

Run	Code values	Real values	Response

	W1	W2	W3	*Kr*	*E*	*Sc*	*Sh* / Wedge	*Sh* / Cone
1	-1	-1	1	1.5	2.5	0.8	1.21146	1.72661
2	-1	0	0	1	1.5	0.8	1.1839	1.88571
3	0	0	0	1	1.5	0.7	1.2245	1.79873
4	-1	-1	-1	1	2.5	0.7	0.00526889	1.76025
5	0	0	0	1	0.5	0.7	1.76235	3.19715
6	0	0	0	1.5	2.5	0.6	0.236285	1.64276
7	0	-1	0	1	1.5	0.7	1.2245	1.79873
8	1	-1	1	0.5	0.5	0.8	0.578401	3.20273
9	1	-1	-1	1	1.5	0.6	0.509385	1.59652
10	1	0	0	1.5	0.5	0.6	1.63875	2.504
11	1	1	1	1.5	1.5	0.7	1.14446	0.596043
12	0	0	-1	1	1.5	0.7	1.2245	1.79873
13	0	0	0	1	1.5	0.7	1.2245	1.79873
14	1	1	-1	1	1.5	0.7	1.2245	1.79873
15	0	0	0	0.5	1.5	0.7	0.521364	1.70754
16	-1	1	1	1.5	0.5	0.8	1.50873	2.83837
17	-1	1	-1	0.5	2.5	0.8	0.42783	1.92299
18	0	0	1	1	1.5	0.7	1.2245	1.79873
19	0	1	0	0.5	2.5	0.6	0.486412	0.947402
20	0	0	0	0.5	0.5	0.6	1.16925	1.79827

Analysis of variance (ANOVA) is used to evaluate the adequacy and realism of the constructed model, with the findings shown in Table 11. parameters that have p-values below 0.05 are considered to have statistical significance, whilst those with larger values are regarded as insignificant. For the wedge, there is no significant statistical link between Sc, Sc2, and the interaction term E*Sc. Similarly, for the cone, Kr, Sc2, and E*Sc are non-significant. The wedge and cone have coefficient of determination (R2) values of 98.57% and 97.76%, respectively, confirming the model's correctness. Further investigation reveals a strong correlation between solutal Sherwood number (Sh) values and the input parameters Kr, E, and Sc of the form:

$$Sh(wedge) = 1.109 + 0.2556Kr - 0.429E - 0.103Kr^2 - 0.052E^2 - 0.108Kr * E + 0.187Kr * Sc$$

(33)

$$Sh(cone) = 1.755 - 0.5541E + 0.3087Sc - 0.538Kr^2 + 0.789E^2 + 0.02Kr * E - 0.245Kr * Sc$$

(34)

Table 11: Analysis of Variance (ANOVA) of Sh.

Source	DF	Adjusted SS		Adjusted MS		F-value		p-value		Coefficient	
		Wedge	Cone	Wedge	Cone	Wedge	Cone	Wedge	Cone	Wedge	Cone
Model	9	3.50145	6.67314	0.38905	0.74146	3.95	8.46	0.022	0.001	-	-
Linear	3	2.56987	4.03031	0.85662	1.34344	8.70	15.33	0.004	0.000	1.109	1.755
Kr	1	0.65353	0.00735	0.65353	0.00735	6.64	0.08	0.028	0.778	0.2556	-0.0271
E	1	1.84060	3.06972	1.84060	3.06972	18.69	35.02	0.002	0.000	-0.4290	-0.5541
Sc	1	0.07573	0.95324	0.07573	0.95324	0.77	10.88	0.401	0.008	0.0870	0.3087
Square	3	0.22339	2.10092	0.07446	0.70031	0.76	7.99	0.544	0.005	-	-
Kr*Kr	1	0.02935	0.79687	0.02935	0.79687	8.30	9.09	0.007	0.013	-0.103	-0.538
E*E	1	0.00755	1.71022	0.00755	1.71022	10.08	19.51	0.027	0.001	-0.052	0.789
Sc*Sc	1	0.02207	0.00716	0.02207	0.00716	0.22	0.08	0.646	0.781	-0.090	0.051
2-Way Interaction	3	0.70820	0.54190	0.23607	0.18063	2.40	2.06	0.129	0.169	-	-
Kr*E	1	0.09382	0.00311	0.09382	0.00311	6.95	0.04	0.035	0.004	-0.108	0.020
Kr*Sc	1	0.27922	0.48110	0.27922	0.48110	12.84	5.49	0.012	0.041	0.187	-0.245
E*Sc	1	0.33516	0.05770	0.33516	0.05770	3.40	0.66	0.095	0.436	0.205	-0.085

Error	10	0.984 80	0.876 49	0.098 48	0.087 65						
Lack-of-Fit	5	0.984 80	0.876 49	0.196 96	0.175 30	*	*	*	*		
Pure Error	5	0.000 00	0.000 00	0.000 00	0.000 00						
Total	19	4.486 26	7.549 62								

Figs. 14 and 15 depict the difference between residual and observation for $Sh\ (wedge)$ and $Sh\ (cone)$.

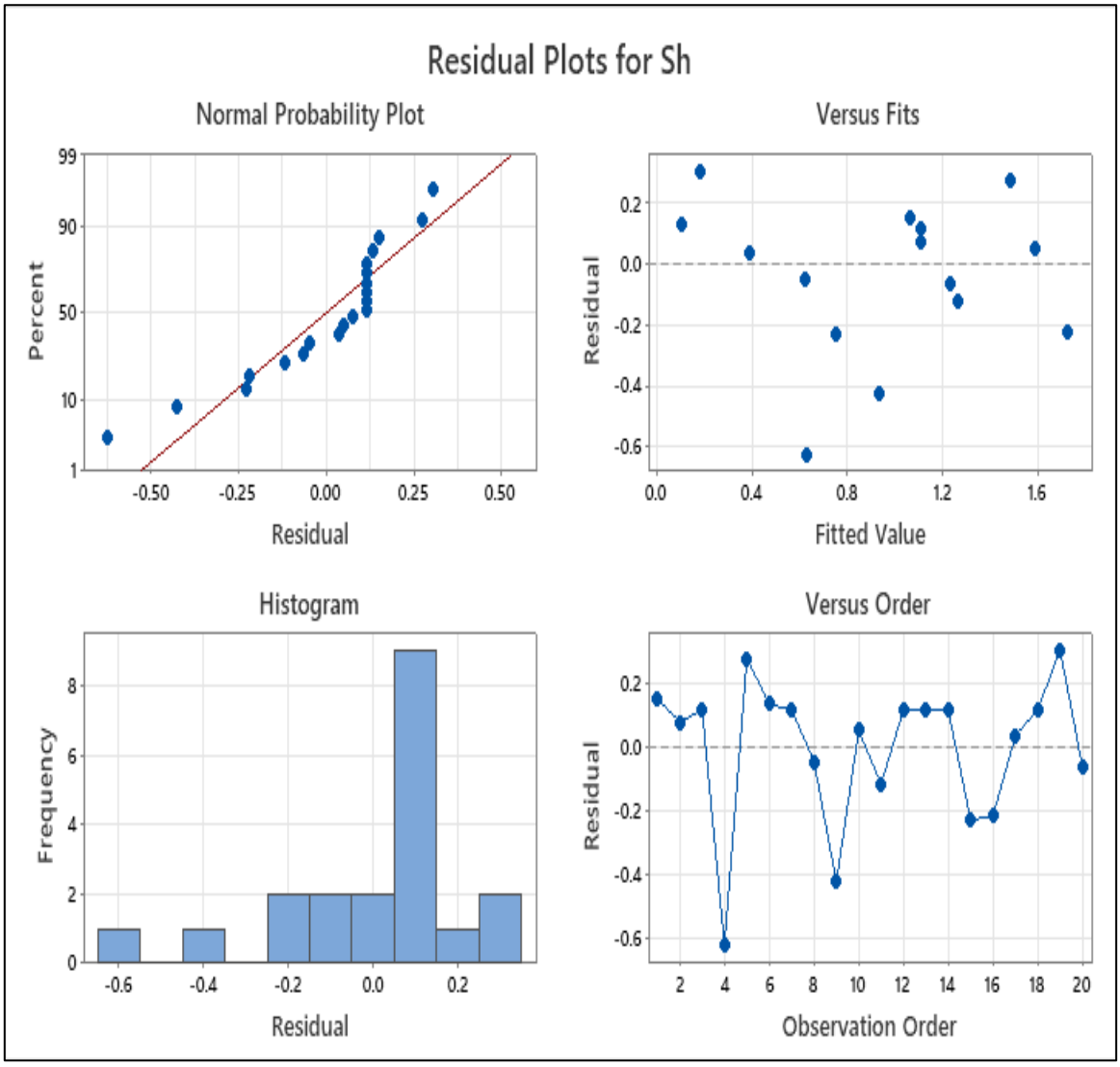


Figure 14: The difference between residual and observation for $Sh\ (wedge)$.

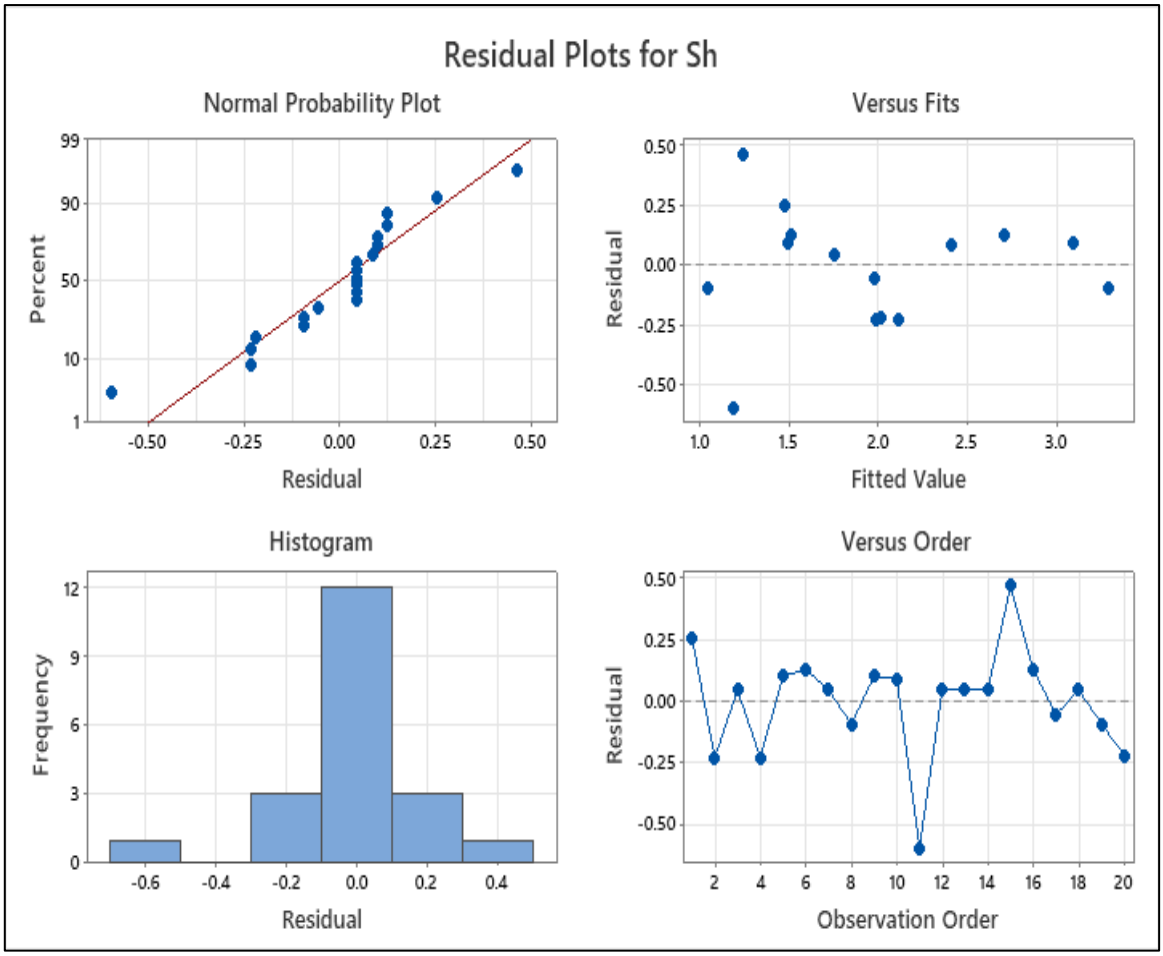


Figure 15: The difference between residual and observation for Sh $(cone)$.

5.4 Impact of Nb, Nt and Le on the nanoparticle Sherwood number (Shn)

Finally, we examine nanoparticle Sherwood number (Shn).

Table 12: The impact of different parameter values for nanoparticle Sherwood number.

Parameter	Symbol	Level		
		-1	0	1
$0.6 \le Nb \le 1.6$	W1	0.6	1.1	1.6
$0.5 \le Nt \le 0.9$	W2	0.5	0.7	0.9
$0.5 \le Le \le 1.5$	W3	0.5	1	1.5

The appropriate correlation is:

$$Shn = J_0 + J_1 Nb + J_2 Nt + J_3 Le + J_{11} Nb^2 + J_{22} Nt^2 + J_{33} Le^2 + J_{12} Nb * Nt + J_{13} Nb * Le + J_{14} Nt * Le \quad (35)$$

Table 13: An approach to research grounded upon CCD.

Run	Code values			Real values			Response	
	W1	W2	W3	*Nb*	*Nt*	*Le*	*Shn* / Wedge	*Shn* / Cone
1	-1	-1	1	0.6	0.9	1.5	1.32672	2.60733
2	-1	0	0	0.6	0.7	1	1.64324	1.67513
3	0	0	0	0.6	0.5	1.5	1.3045	1.68561
4	-1	-1	-1	1.1	0.7	1	0.920182	1.6575
5	0	0	0	1.6	0.7	1	1.0823	1.61582
6	0	0	0	1.1	0.9	1	1.0522	1.58775
7	0	-1	0	1.1	0.7	1.5	0.721933	1.56931
8	1	-1	1	1.1	0.7	1	0.920182	1.6575
9	1	-1	-1	1.1	0.7	1	0.920182	1.6575
10	1	0	0	1.6	0.5	0.5	0.419261	0.250753
11	1	1	1	1.6	0.9	1.5	2.79985	2.87089
12	0	0	-1	1.6	0.9	0.5	0.413078	0.242447
13	0	0	0	1.1	0.7	1	0.920182	1.6575
14	1	1	-1	1.1	0.7	0.5	0.404837	0.234846
15	0	0	0	1.1	0.7	1	0.920182	1.6575
16	-1	1	1	0.6	0.5	0.5	0.392905	0.22252
17	-1	1	-1	1.1	0.5	1	0.911149	1.5978
18	0	0	1	0.6	0.9	0.5	0.196459	0.869101
19	0	1	0	1.1	0.7	1	0.920182	1.6575
20	0	0	0	1.6	0.5	1.5	0.388664	0.250753

The validity and practical relevance of the proposed model are assessed using an ANOVA, with the results summarised in Table 14. Parameters with p-values less than 0.05 are deemed statistically significant, whereas those over this level are regarded as inconsequential. For the wedge design, Nb, Nt2, and the interaction term Nb*Le are not statistically significant. In the cone configuration, Nb, Nt2, Nb*Nt, and Nb*Le are considered irrelevant. The model's high R2 values (99.04% for the wedge and 98.56% for the cone) shows its trustworthiness. A more detailed statistical study reveals a significant link between the Sherwood number for nanoparticles (Shn) and the input variables Nb, Nt and Le via the relations:

$$Shn(wedge) = 7.20 - 2.59Nt + 2.87Le + 3.07Nb^2 - 0.33Le^2 - 3.58Nb * Nt - 4.58Nt * Le \quad (36)$$

$$Shn(cone) = 14.39 + 1.44Nt - 0.05Le + 1.65Nb^2 - 4.71Le^2 - 0.89Nt * Le \quad (37)$$

Table 14: Analysis of Variance (ANOVA) of Shn.

Source	DF	Adjusted SS		Adjusted MS		F-value		p-value		Coefficient	
		Wedge	Cone	Wedge	Cone	Wedge	Cone	Wedge	Cone	Wedge	Cone
Model	9	5.14674	10.0618	0.57186	1.11797	4.92	9.01	0.010	0.001	-	-
Linear	3	2.79153	7.2061	0.93051	2.40204	8.01	19.35	0.005	0.000	7.20	14.39
Nb	1	0.00573	0.3345	0.00573	0.33453	0.05	2.69	0.829	0.132	4.91	2.80
Nt	1	0.56256	1.7390	0.56256	1.73896	14.84	14.01	0.005	0.004	-2.59	1.44
Le	1	2.22324	5.1326	2.22324	5.13261	19.14	41.34	0.001	0.000	2.87	-0.05
Square	3	0.64272	1.6247	0.21424	0.54155	1.84	4.36	0.203	0.033	-	-
Nb*Nb	1	0.40461	0.0258	0.40461	0.02583	13.48	19.21	0.002	0.008	3.07	1.65
Nt*Nt	1	0.00002	0.0054	0.00002	0.00538	0.00	0.04	0.991	0.839	-1.32	-3.02
Le*Le	1	0.47547	1.1493	0.47547	1.14932	14.09	9.26	0.007	0.012	-0.33	-4.71
2-Way Interaction	3	1.71249	1.2310	0.57083	0.41033	4.91	3.31	0.024	0.066	-	-
Nb*Nt	1	0.83155	0.1361	0.83155	0.13612	7.16	1.10	0.023	0.320	-3.58	-1.38
Nb*Le	1	0.01235	0.0410	0.01235	0.04102	0.11	0.33	0.751	0.578	7.25	0.82
Nt*Le	1	0.86859	1.0538	0.86859	1.05385	7.48	8.49	0.021	0.015	-4.54	-0.89
Error	10	1.16174	1.2415	0.11617	0.12415						
Lack-of-Fit	5	1.16174	1.2415	0.23235	0.24829	*	*	*	*		
Pure Error	5	0.00000	0.0000	0.000	0.00000						
Total	19	6.30847	11.3032								

Figs. 16 and 17 depict the difference between residual and observation for $Shn\ (wedge)$ and $Shn\ (cone)$.

Figure 16: The difference between residual and observation for Shn $(wedge)$.

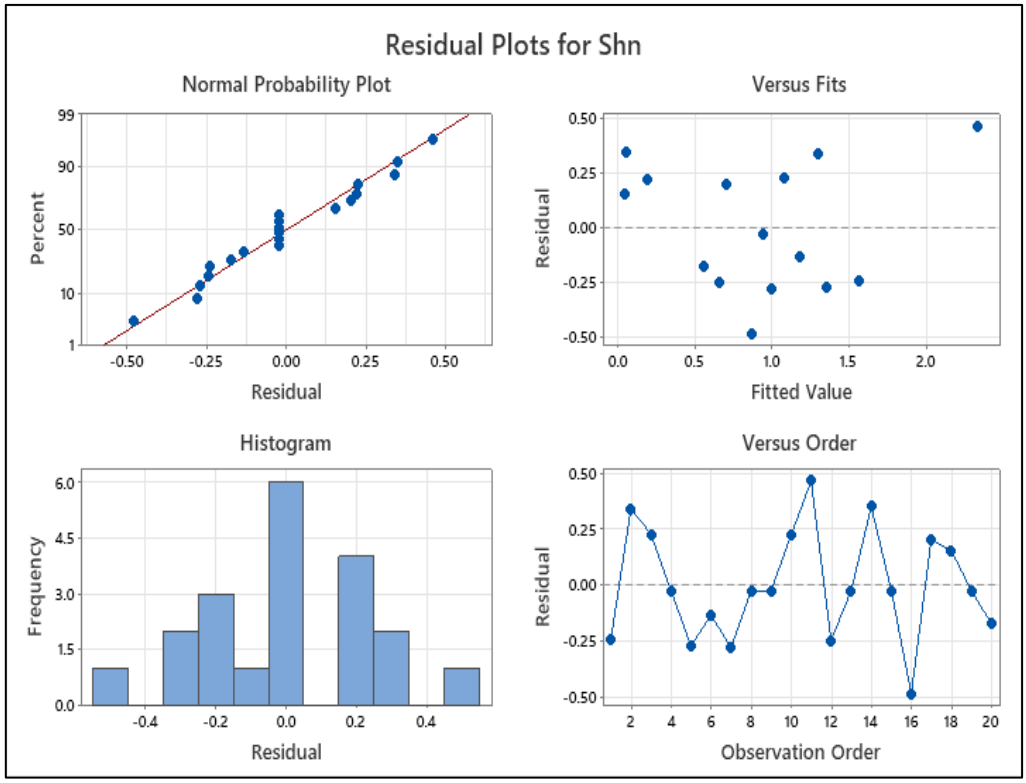
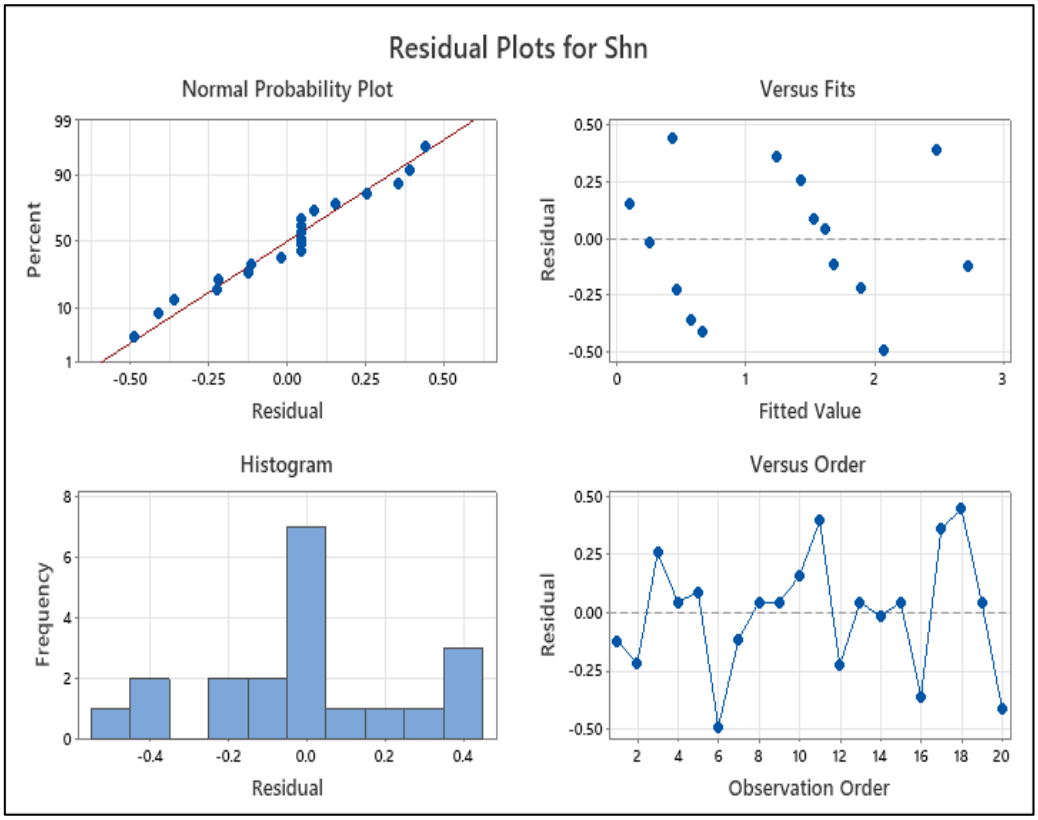


Figure 17: The difference between residual and observation for $Shn(cone)$.



The residual plots for Cf, Nu, Sh and Shn for the wedge and cone designs are shown in Figures 10–17. A normal (Gaussian) distribution for the residuals would be supported by the positive trend shown in the regression probability charts. Furthermore, there seems to be some structure in the greatest residuals, and the residual histograms have a very even distribution. It is clear that the suggested model works and provides a decent match when looking at the residuals' distribution and behaviour as a whole. All four response variables, Cf, Nu, Sh and Shn, are adequately captured by the quadratic model used in this statistical study.

6. CONCLUSIONS

A theoretical and numerical study of electro-conductive functional magnetic nanofluid boundary layer flow external to both wedge and cone shapes embedded in porous media under external magnetic field modulation has been presented. Chemical reaction, thermal radiation, heat generation and activation energy effects have been featured in the mathematical model. Buongiorno's two-component nanoscale model has been deployed to evaluate mass diffusion phenomena of the nanoparticles with thermophoretic and Brownian motion effects. A separate species equation has been included for reactive solute diffusion. The transformed nonlinear ordinary differential boundary value problem has been solved with the MATLAB bvp4c method. Validation has been included with earlier studies neglecting nanoparticle and heat generation effects. Response Surface Methodology (RSM) has been utilized to conduct statistical analysis and optimize the transport process for skin friction, Nusselt number (heat transfer rate), solutal Sherwood number (solute mass transfer rate) and nanoparticle Sherwood number. The main findings of the present study can be summarized as follows:

(i) Increasing Richardson number (Ri) depletes velocity field and produces enhanced control of the coating enabling homogeneity to be achieved in surface finishing with thinner hydrodynamic boundary layers. For both the cone and wedge geometries, flow acceleration is produced with decreasing Richardson numbers.

(ii) An elevation in activation energy parameter (E) opposes solute mass diffusion and produces a reduction in solute concentration and thinner solutal boundary layers.

(iii) An increase in homogenous destructive chemical reaction parameter (Kr) depletes the solute concentration.

(iv) Higher solute concentration magnitudes are produced for the wedge geometry relative to the cone geometry.

(v) Increasing Brownian motion parameter (Nb) suppresses the nanoparticle volume fraction (concentration), altering the nanocoating properties.

(vi) Increasing Brownian motion parameter (Nb) generates strong micro-convection currents in the base fluid, increasing the overall thermal conductivity and enhancing temperature and associated thermal boundary layer thickness.

(vii) Increasing thermophoresis parameter (Nt) intensifies thermal diffusion and elevates temperatures.

(viii) Increasing thermophoresis parameter (Nt) reduces nanoparticle volume fraction and decreases nanoparticle species boundary layer thickness.

(ix) An elevation in heat generation (source) parameter (Q) strongly accentuates temperature magnitudes with larger values computed for the wedge case compared with the cone case. A sharper rate of temperature descent from the substrate surface accompanies the cone case relative to the wedge case.

(x) Increasing radiation-conduction parameter (R) boosts the temperature values in the regime and higher magnitudes are obtained for the wedge case.

(xi) Increasing nanoparticle species buoyancy parameter (Nr) assists momentum diffusion, elevates velocity and reduces hydrodynamic boundary layer thickness.

(xii) Higher values of solutal buoyancy parameter (Nc) oppose momentum diffusion, decrease velocity magnitudes and increase momentum boundary layer thickness.

(xiii)Increasing permeability parameter for the porous medium (K) manifests in a decrease in, actual permeability and a boost in quantity of solid fibers. This circumvents nanofluid percolation, increases Darcian drag and decreases velocity magnitude.

(xiv) An elevation in modified Hartmann magnetic number (M) produces a ramp up in Lorentzian magnetic drag which cause nanoparticles to align and form chain-like structures and strongly damps the flow.

(xv) The skin friction, Nusselt number, solutal Sherwood number, and nanoparticle Sherwood number regression models based on RSM all attain excellent accuracies for the wedge design, with R^2 values of 99.73%, 99.85%, 98.57%, and 99.04%, respectively.

(xvi) Strong predictive performance is indicated via RSM simulations by the equivalent R2 values of 98.45% for skin friction, 97.65% for the Nusselt number, 97.76% for the Sherwood number, and 98.56% for the nanoparticle Sherwood number for the case of a cone.

The current simulations have demonstrated that MATLAB and RSM are powerful methodologies for modelling complex nanofluid coating flows. Future studies may explore additional multi-physics including phase change (melting) [56, 57], non-Newtonian behaviour e.g. micropolar coatings [58], Marangoni surface-tension effects [59], catalytic reactions [60] and ferromagnetic nanofluids [61]. Efforts in these directions are underway and will be communicated soon.

ACKNOWLEDGEMENTS: The author would like to thank GITAM Deemed to be University for providing the MATLAB Software.

FUNDING: No funding was received by any agency for this work.

DATA AVAILABILITY STATEMENT: This article contains all the pertinent data generated or analysed during this investigation; further material can be provided upon reasonable request to the authors.

DECLARATION: We, the authors of this manuscript declare that this work is original and has not been published or submitted elsewhere for consideration.

CONFLICT OF INTEREST: The author declares that there is no conflict of interest.

REFERENCES

[1] Hongze Yin, Wengang Chen, Dongsheng Xia, Huajie Wu, Peiyao Jing, Long Chen, Luzhong Zhang, Yuhao Wang, Zexiao Wang, Dongyang Li, Friction properties of graphite coating deposited on wedge-shaped textured aluminum alloys prepared by 3D printing, Journal of Materials Research and Technology, Volume 20, 2022, Pages 4452-4472.

[2] Hsu C-C. Viscoelastic flow past a wedge with a soluble coating. Journal of Fluid Mechanics. 27(3):445-463 (1967).

[3] M.M. Rashidi, O. Anwar Bég and M.T. Rastegari, A study of non-Newtonian flow and heat transfer over a non-isothermal wedge using the homotopy analysis method, Chemical Engineering Communications, 199:2, 231-256 (2012).

[4] E. Takeuchi, F. Negrini, M. Fabbri, M. Tani, M. Zuccarini, Electromagnetic control of the meniscus shape during casting in a high-frequency magnetic field, Energy Conv Mgmt., 41 (15) 1678-1701 (2000).
[5] S. Constantinides, Chapter 11 - Permanent magnet coatings and testing procedures, Editor(s): John Croat, John Ormerod, Series in Electronic and Optical Materials, Modern Permanent Magnets, Woodhead Publishing, (2002) 371-402.

[6] Hans-Joachim Streitberger (Author) Artur Goldschmidt(Author), BASF Handbook Basics of Coating Technology, BASF, Germany (2018).

[7] K. Vajravelu and J. Nayfeh, Hydromagnetic convection at a cone and a wedge, International Communications in Heat and Mass Transfer, vol. 19, no. 5, pp. 701–710 (1992). doi: 10.1016/0735-1933(92)90052-J.

[8] A. J. Chamkha, Non-Darcy hydromagnetic free convection from a cone and a wedge in porous media, International Communications in Heat and Mass Transfer, vol. 23, no. 6, pp. 875–887 (1996).

[9] S. Abdul Gaffar, V. Ramachandra Prasad, S. Keshava Reddy, O. Anwar Bég, Magnetohydrodynamic free convection boundary layer flow of non-Newtonian tangent hyperbolic fluid from a vertical permeable cone with variable surface temperature, J. Braz. Society Mech. Sci. Eng., 39:101–116 (2017).

[10] S. A.Gaffar, V. R. Prasad, B. Vijaya and O. Anwar Bég, Mixed convection flow of magnetic viscoelastic polymer from a non-isothermal wedge with Biot number effects, Int. J. Engineering Mathematics, Volume 2015, Article ID 287623, 15 pages (2015).

[11] Abdeen DH, El Hachach M, Koc M, Atieh MA. A review on the corrosion behaviour of nanocoatings on metallic substrates. Materials (Basel). 12 (2): 210 (2019). doi: 10.3390/ma12020210

[12] Razzaq, Izzat et al., Nanofluids for advanced applications: a comprehensive review on preparation methods, properties, and environmental impact, ACS Omega (2025) 10, 6, 5251–5282.

[13] J. Buongiorno, Convective transport in nanofluids, ASME J. Heat Transfer, 128 (2006) 240–250.

[14] S.U.S. Choi, D.A. Singer, H.P. Wang (Eds.), Enhancing thermal conductivity of fluids with nanoparticle, Development and application of non-Newtonian flows, vol. FED 231, ASME, New York (1995), pp. 99-105.

[15] R.J. Tiwari, M.K. Das, Heat transfer augmentation in a two-sided lid-driven differentially heated square cavity utilizing nanofluids, Int. J. Heat. Mass Transf., 50 (2007), pp. 2002-2018.

[16] O. Anwar Bég, Nonlinear multi-physical laminar nanofluid bioconvection flows: Models and computation, A. Sohail, Z. Li (Eds.): Computational Approaches in Biomedical Nano-Engineering, Wiley, Chapter 5, pp. 113-145 (2018). ISBN: 3527344721, 9783527344727

[17] Weitao Huang, Mumin Rao, Sizhe Chen, Jiayi Deng, Yabei Zhang, Chi Yu, Fa-Qian Liu, Synergistic antifouling performance of Cu/MXene composite nanofluid-infused SLIPS coatings with self-cleaning and self-replenishing capabilities for marine applications, Progress in Organic Coatings, Volume 215,2026,110104.

[18] Sun X, Gu S, Wang L, Wang H, Xiong S, Yin X, Yang S. Multifunctional liquid-like magnetic nanofluids mediated coating with anticorrosion and self-healing performance. J Colloid Interface Sci. 2024 Jan 15;654(Pt A):25-35. doi: 10.1016/j.jcis.2023.09.182.

[19] P. Poornima Vijayan, Archana Somadas Radhamany, Ansar Ereath Beeran, Maryam Jouyandeh, Mohammad Reza Saeb, Chapter 16 - Magnetic nanoparticles-based coatings, Editor(s): Huaihe Song, Tuan Anh Nguyen, Ghulam Yasin, Nakshatra Bahadur Singh, Ram K. Gupta, In Micro and Nano Technologies, Nanotechnology in the Automotive Industry, Elsevier, 2022, Pages 317-343.

[20] L. Pengpeng, F. Xue, L. Xin, X. Li, Y. Fan, J. Zhao, L. Tian, J. Sun, L. Ren, Anticorrosion Coating with Heterogeneous Assembly of Nanofillers Modulated by a Magnetic Field, ACS Appl. Mater. Inter. 15 (5) (2023) 7538–7551.

[21] R. S. R. Gorla, A. Chamkha, and A. M. Rashad, Mixed convective boundary layer flow over a vertical wedge embedded in a porous medium saturated with a nanofluid, in 2010 3rd International Conference on Thermal Issues in Emerging Technologies Theory and Applications, IEEE, Dec. 2010, 19-22 December 2010, Cairo, Egypt, pp. 445–451. doi: 10.1109/THETA.2010.5766429.

[22] J. C. Umavathi, Mahesh Ashok Kumar and O. Anwar Bég, Computation of micropolar nanofluid from a wedge with heterogeneous carbon/metallic nanoparticles, viscous dissipation and heat sink/source: Rheological nanocoating flow simulation, Int. J. Modelling and Simulation (USA). (2023) doi.org/10.1080/02286203.2023.2237846 (17 pages).

[23] A. J. Chamkha, S. Abbasbandy, A. M. Rashad, and K. Vajravelu, Radiation effects on mixed convection over a wedge embedded in a porous medium filled with a nanofluid, Transp. Porous Media, vol. 91, no. 1, pp. 261–279, Jan. 2012, doi: 10.1007/s11242-011-9843-5.

[24] N. Sandeep and M. G. Reddy, Heat transfer of nonlinear radiative magnetohydrodynamic Cu-water nanofluid flow over two different geometries, J. Mol. Liq, vol. 225, pp. 87–94, Jan. 2017, doi: 10.1016/j.molliq.2016.11.026.

[25] S. Manjunatha, J. S. Kumar, M. Veera Krishna, and S. V. K. Varma, "ANN modelling on heat and mass transfer in MHD chemically reactive and radiative flow of hybrid ferrofluid over a non-linear stretching porous surface," Multiscale and Multidisciplinary Modeling, Experiments and Design, vol. 8, no. 6, 2025, doi: 10.1007/s41939-025-00879-z.

[26] A. K. Ray, B Vasu, O. Anwar Bég, R. S R Gorla and P. V. S. N. Murthy, Homotopy semi-numerical modelling of non-Newtonian nanofluid transport external to multiple geometries using a revised Buongiorno model, Inventions, 4, 54, 1-27 (2019). doi:10.3390/inventions4040054 (2019).

[27] S. O. Salawu, T. A. Yusuf, E. O. Fatunmbi, and A. M. Obalalu, Dynamics of tri-hybridized Prandtl-Eyring thermal water-based magnetonanofuids flow over double stretched wedge

sheets experiencing force convection, Forces in Mechanics, vol. 15, p. 100270, May 2024, doi: 10.1016/j.finmec.2024.100270.

[28] Xiang Liu, Ping Lan, Ning Lin, Curing reactions of epoxy powder coatings in perspectives of chemical mechanisms and strategies, Prog. Organic Coatings, Volume 199, 2025, 108956.

[29] N. A. Zainal, R. Nazar, K. Naganthran, and I. Pop, Flow and heat transfer over a permeable moving wedge in a hybrid nanofluid with activation energy and binary chemical reaction, Int J Numer Methods Heat Fluid Flow, vol. 32, no. 5, pp. 1686–1705, Apr. 2022, doi: 10.1108/HFF-04-2021-0298.

[30] V. Singh, N. B. Naduvinamani, K. Vinutha, B. C. Prasannakumara, J. K. Madhukesh, and A. Abdulrahman, Sodium alginate-based MHD ternary nanofluid flow across a cone and wedge with exothermic/endothermic chemical reactions: A numerical study, Numer. Heat Transfer A-Appl, pp. 1–20, May 2024, doi: 10.1080/10407782.2024.2355520.

[31] M. V. Krishna and B. P. Reddy, Thermal radiation, heat source, and chemical reaction impacts on MHD convective flow of Casson fluid past an infinite inclined oscillating vertical porous plate, Multiscale and Multidisciplinary Modeling, Experiments and Design, vol. 8, no. 3, p. 196, Mar. 2025, doi: 10.1007/s41939-025-00774-7.

[32] H. Al-Shammari, Z. Ullah, Y. M. Mahrous, M. S. Aldhabani, M. Ahmed Said, S. Al Arni, A. A. Faqihi and N. B. Khedher, Arrhenius activation energy and thermal radiation effects on oscillatory heat-mass transfer of Darcy Forchheimer nanofluid along heat generating cone, Case Studies in Thermal Engineering, vol. 57, p. 104294, May 2024, doi: 10.1016/j.csite.2024.104294.

[33] L. Zhang, M. M. Bhatti, A. Shahid, R. Ellahi, O. Anwar Bég and Sadiq M. Sait, Nonlinear nanofluid fluid flow under the consequences of Lorentz forces and Arrhenius kinetics through a permeable surface: A robust spectral approach, J. Taiwan Inst. Chemical Engineers (2021). doi.org/ 10.1016/j.jtice.2021.04.065 (8 pages).

[34] M. Shanmugapriya, A. S. A. Jeffrey, and R. Sundareswaran, Heat and mass transfer of boundary layer Jeffrey ternary hybrid nanofluid flow over porous wedge with surface-catalysed chemical reactions: An ANFIS Model, Journal of Mathematics, vol. 2024, no. 1, Jan. 2024, doi: 10.1155/2024/7733414.

[35] G. Li, S. Abdal, B. Zhang, N. A. Shah, and Z. Fatima, Bioconvection for Riga wedge flow of tangent hyperbolic nanofluids in the presence of activation energy and mass suction, J. Therm Anal Calorim, Apr. 2025, doi: 10.1007/s10973-025-14051-9.

[36] Patil PM, Doddagoudar SH, Hiremath PS. Convective nanofluid flow over a vertical cone with a rough surface. Heat Transfer. 2022; 51: 3126-3141. doi:10.1002/htj.22440

[37] S. P. Singh, H. Upreti, and M. Kumar, Flow and heat transfer assessment in magnetized Darcy-Forchheimer flow of Casson hybrid nanofluid through cone, wedge, and plate, Bionanoscience, vol. 14, no. 1, pp. 395–408, Mar. 2024, doi: 10.1007/s12668-023-01253-4.

[38] H. B. Santhosh, M. S. Upadhya, N. A. Ahammad, C. S. K. Raju, N. A. Shah, and W. Weera, Comparative analysis of a cone, wedge, and plate packed with microbes in non-Fourier heat flux, Mathematics, vol. 10, no. 19, p. 3508, Sep. 2022, doi: 10.3390/math10193508.

[39] Song, H. (2018). Fundamentals of Fluid Mechanics Through Porous Media. In: Engineering Fluid Mechanics. Springer, Singapore.

[40] Ding, X. and Harris, T.A.L. (2017), Review on penetration and transport phenomena in porous media during slot die coating. J. Polym. Sci. Part B: Polym. Phys., 55: 1669-1680. https://doi.org/10.1002/polb.24307

[41] Padmaja K, B Rushi Kumar, O. Anwar Bég and T. A. Bég, Mathematical modelling of Cu − H2O magnetic nanofluid flow with higher order chemical reaction and cross diffusion from a rotating vertical cone adjacent to a porous medium: application to magnetic nano-coatings, J. Multiscale Modelling (2023) 2350006 (21 pages) DOI: 10.1142/S1756973723500063.

[42] Md. Jashim Uddin, N.H. Md. Yusoff, O. Anwar Beg and Ahamd Izani Ismail, Lie group analysis and numerical solutions for non-Newtonian nanofluid flow in a porous medium with internal heat generation, Physica Scripta, 87 (2013) 025401 (14pp).

[43] O. Anwar Bég, V. R. Prasad, B. Vasu and R.S.R. Gorla, Computational modelling of magnetohydrodynamic convection from a rotating cone in orthotropic Darcian porous media, J. Braz. Society Mech Sci Eng, 39, 2035–2054 (2017).

[44] Venkatadri, K., Sree Harshitha, P., Beg, O. Anwar and S. Kuharat, Numerical study of hybrid binary Al2O3-Cu-H2O nanofluid coating boundary layer flow from an exponentially stretching/shrinking perforated substrate with Cattaneo-Christov heat flux, heat source, suction and multiple slip effects. Numerical Heat Transfer, Part B: Fundamentals, 86(9), 2978–3001 (2025).

[45] B. Mahanthesh et al., Response surface optimization of heat transfer rate in Falkner-Skan flow of ZnO − EG nano-liquid over a moving wedge: Sensitivity analysis, International Communications in Heat and Mass Transfer, Volume 125, 2021, 105348.

[46] A. Hussain, N. Farooq, A. Ahmad, and L. Sarwar, Impact of double diffusivity on the hyperbolic tangent model conveying nano fluid flow over the wedge, International Communications in Heat and Mass Transfer, vol. 145, p. 106849 (2023). doi: 10.1016/j.icheatmasstransfer.2023.106849.

[47] I. A. Hassanien, A. A. Abdullah, and R. S. R. Gorla, Flow and heat transfer in a power-law fluid over a non-isothermal stretching sheet, Math Comp. Model., vol. 28, no. 9, pp. 105–116, 1998, doi: 10.1016/S0895-7177(98)00148-4.

[48] M. Kulkarni, Influence of activation energy and multi-diffusive quadratic convective nanoliquid flow past a cone and wedge, International Communications in Heat and Mass Transfer, 157, p. 107797 (2024). doi: 10.1016/j.icheatmasstransfer.2024.107797.

[49] S. Manjunatha et al., Thermal radiation and thermo-diffusion in Casson-ferrofluid over a magnetized porous surface: RSM analysis, International Journal of Thermofluids, vol. 26, p. 101130, Mar. 2025, doi: 10.1016/j.ijft.2025.101130.

[50] K. Venkatadri, Hakan F. Öztop, V. Ramachandra Prasad, S. Parthiban and O. Anwar Bég, RSM-based sensitivity analysis of hybrid nanofluid MHD flow in an enclosure filled with non-

Darcy porous medium using the Lattice Boltzmann Method, Numerical Heat Transfer - A (2023). doi.org/10.1080/10407782.2023.2193708

[51] S. Manjunatha, J. S. Kumar, and S. V. K. Varma, "Impacts of heat generation and buoyancy forces on hyperbolic tangent magneto ferrofluid flow with Darcy–Forchheimer model over a nonlinear stretching sheet: RSM analysis," The European Physical Journal Plus, vol. 140, no. 6, p. 577, 2025, doi: 10.1140/epjp/s13360-025-06477-9.

[52] K. Nirisha, M. K. Mishra, V. Nagaradhika, R. Sharma, O. Anwar Bég and Ankur Singh, A statistical analysis of the non-Newtonian nanofluid flow model in a single-phase squeezing channel, Int. J. Applied and Computational Mathematics, Int. J. Appl. Comp. Math (2025) 11:182. (21 pages). https://doi.org/10.1007/s40819-025-02009-2 (2025).

[53] K. Nirisha, Nagaradhika V, S. Sreedhar, Manjunatha S, S Ramesh, O Anwar Bég, Modeling Joule heating in magnetized porous structures using statistical techniques, Mechanics of Time-Dependent Materials, (2025) 29:53 (28 pages). https://doi.org/ 10.1007/s11043-025- 09793-w

[54] K. Nirisha, V. Nagaradhika, Manjunatha S and O. Anwar Bég, Statistical analysis of MHD Darcy–Forchheimer Sisko Hybrid nanofluid flow over a bilinear stretching sheet with heat and mass transfer effects, Journal of Thermal Engineering (2026). In press.

[55] Anderson, M.J. and Whitcomb, P.J. RSM simplified: Optimizing Processes using Response Surface Methods for Design of Experiments. 2016. Productivity Press, New York, USA.

[56] Ahmadi Azar A. et al. Analytical solution for MHD nanofluid flow over a porous wedge with melting heat transfer. Heliyon. (2024) 22; 10(15): e34888.

[57] Adnan et al. (2025), Challenging thermal mechanisms in nanofluid wedge flow over a melting surface: applications of Al2O3 and CuO nanomaterials, Multidiscipline Modelling in Materials and Structures, Vol. 21 No. 6 pp. 1513–1528.

[58] O. Anwar Bég, B. Vasu, Atul Kumar Ray, T.A. Bég, Ali Kadir, Henry J. Leonard and R.S.R. Gorla, Homotopy simulation of dissipative micropolar flow and heat transfer from a two-dimensional body with heat sink effect: applications in polymer coating, Chem. Biochem. Eng. Quart. 34 (4) 257–275 (2020).

[59] MD. Shamshuddin, S.R. Mishra, O. Anwar Bég, T.A. Bég and Ali Kadir, Computation of radiative Marangoni (thermocapillary) magnetohydrodynamic convection in Cu-water based

nanofluid flow from a disk in porous media: smart coating simulation, Heat Transfer (2020). DOI: 10.1002/htj.21963 (20 pages)

[60] P.K. Pattnaik, S. R. Mishra, O. Anwar Bég, et al. Axisymmetric radiative titanium dioxide magnetic nanofluid flow on a stretching cylinder with homogeneous/heterogeneous reactions in Darcy-Forchheimer porous media: intelligent nanocoating simulation, Materials Science and Engineering B (2021). doi.org/10.1016/j.mseb.2021.115589 (26 pages)

[61] S.O. Solawu, M. Shamshuddin, O. Anwar Bég, Influence of magnetization, variable viscosity and thermal conductivity on Von Karman swirling flow of H2O-Fe3O4 and H2O-Mn-ZNFe2O4 ferromagnetic nanofluids from a stretchable rotating disk: smart spin coating simulation, Materials Science and Engineering B (USA). 279 (2022) 115659 (13 pages).